Astronomy & Astrophysics

An elliptical accretion disk following the tidal disruption event AT 2020zso

T. Wevers[1], M. Nicholl[2], M. Guolo[1,3], P. Charalampopoulos[4], M. Gromadzki[5], T. M. Reynolds[6], E. Kankare[6],
G. Leloudas[4], J. P. Anderson[1], I. Arcavi[7,8], G. Cannizzaro[9,10], T.-W. Chen[11], N. Ihanec[5], C. Inserra[12],
C. P. Gutiérrez[13,14], P. G. Jonker[9,10], A. Lawrence[15], M. R. Magee[16], T. E. Müller-Bravo[17], F. Onori[18],
E. Ridley[3], S. Schulze[19], P. Short[15], D. Hiramatsu[20,21,22], M. Newsome[20,21], J. H. Terwel[23],
S. Yang[11], and D. Young[24]

(Affiliations can be found after the references)

ABSTRACT

Aims. The modelling of spectroscopic observations of tidal disruption events (TDEs) to date suggests that the newly formed accretion disks are mostly quasi-circular. In this work we study the transient event AT 2020zso, hosted by an active galactic nucleus (AGN; as inferred from narrow emission line diagnostics), with the aim of characterising the properties of its newly formed accretion flow.

Methods. We classify AT 2020zso as a TDE based on the blackbody evolution inferred from UV/optical photometric observations and spectral line content and evolution. We identify transient, double-peaked Bowen (N III), He I, He II, and Hα emission lines. We model medium-resolution optical spectroscopy of the He II (after careful de-blending of the N III contribution) and Hα lines during the rise, peak, and early decline of the light curve using relativistic, elliptical accretion disk models.

Results. We find that the spectral evolution before the peak can be explained by optical depth effects consistent with an outflowing, optically thick Eddington envelope. Around the peak, the envelope reaches its maximum extent (approximately 10^{15} cm, or ∼3000–6000 gravitational radii for an inferred black hole mass of $5-10 \times 10^5 \, M_\odot$) and becomes optically thin. The Hα and He II emission lines at and after the peak can be reproduced with a highly inclined ($i = 85 \pm 5$ degrees), highly elliptical ($e = 0.97 \pm 0.01$), and relatively compact (R_{in} = several $100 \, R_g$ and R_{out} = several $1000 \, R_g$) accretion disk.

Conclusions. Overall, the line profiles suggest a highly elliptical geometry for the new accretion flow, consistent with theoretical expectations of newly formed TDE disks. We quantitatively confirm, for the first time, the high inclination nature of a Bowen (and X-ray dim) TDE, consistent with the unification picture of TDEs, where the inclination largely determines the observational appearance. Rapid line profile variations rule out the binary supermassive black hole hypothesis as the origin of the eccentricity; these results thus provide a direct link between a TDE in an AGN and the eccentric accretion disk. We illustrate for the first time how optical spectroscopy can be used to constrain the black hole spin, through (the lack of) disk precession signatures (changes in inferred inclination). We constrain the disk alignment timescale to >15 days in AT2020zso, which rules out high black hole spin values ($a < 0.8$) for $M_{BH} \sim 10^6 \, M_\odot$ and disk viscosity $\alpha \gtrsim 0.1$.

Key words. accretion, accretion disks – galaxies: active – quasars: supermassive black holes

1. Introduction

Double-peaked emission lines, usually seen in H Balmer and He II optical transitions, are observed in a small fraction (∼3%) of active galactic nuclei (AGNs; Chen et al. 1989; Chen & Halpern 1989; Eracleous & Halpern 1994; Strateva et al. 2003). Although a number of possible explanations for their origin exist in the literature, including binary supermassive black holes (SMBHs; Begelman et al. 1980; Gaskell et al. 1983), bipolar outflows (Norman & Miley 1984; Zheng et al. 1990), or highly anisotropic continuum sources (Goad & Wanders 1996), the leading explanation is that they originate in the outer parts of an inclined accretion disk (several thousand gravitational radii, where the gravitational radius $R_g = \frac{GM_{BH}}{c^2}$; see e.g. Eracleous & Halpern 2003 for a detailed discussion).

The original literature models (e.g. Chen et al. 1989; Chen & Halpern 1989) envisaged a circular accretion disk and were successful in reproducing ∼40% of the known samples (Eracleous & Halpern 1994; Strateva et al. 2003). The observed sample morphology of double-peaked AGNs is diverse, including both stronger blue than red peaks and vice versa (see e.g. Eracleous & Halpern 2003 for an overview); the latter in particular cannot be explained with a circular accretion disk model

alone. Some show line profile variability, observed on timescales from a few days (the 'reverberation' timescale; Schimoia et al. 2015) up to months and years (the 'dynamical' timescale; e.g. Gezari et al. 2007; Schimoia et al. 2017). Motivated by this diverse behaviour, more sophisticated and, more importantly, non-axisymmetric accretion disk models were developed (Eracleous et al. 1995; Strateva et al. 2003). Such elliptical models were able to reproduce the majority (but again, not all) of the sources where the circular models failed.

Two main hypotheses were put forward by Eracleous et al. (1995) for the formation of such eccentric accretion disks around SMBHs: binary SMBHs, where the eccentricity of the disk is pumped by the tidal torques of the secondary; and tidal disruption events (TDEs), in which the formation of a highly eccentric structure is a natural expectation in the absence of a mechanism to efficiently and rapidly remove angular momentum from the stellar debris. The vastly different timescales involved provide a mechanism to discriminate between these hypotheses through spectroscopic monitoring. In particular, binary SMBH disks are expected to evolve in thousands of years, whereas in TDEs evolution can be expected on timescales of weeks to months.

There are some previous claims in the literature for the presence of disks with significant eccentricity following TDEs.

Cao et al. (2018) model the prototypical TDE ASASSN–14li, finding a large disk ($r_{out} \sim 1700\,R_g$) and an eccentricity $e = 0.97$. However, the profiles in this event are single-peaked and, moreover, can also be modelled as an optically thick, spherically symmetric outflow, where the line evolution is explained through electron scattering depth variations (Roth & Kasen 2018). Given the absence of significant asymmetries and double-peaked profiles, the evidence for an accretion disk origin of the emission lines is unclear. Using the same model, Liu et al. (2017) modelled the TDE PTF–09djl (see also Arcavi et al. 2014); for this source the data are sparse and noisy, but the Hα line does appear strongly asymmetric. It can be fit with a compact, highly elliptical ($e = 0.96$) accretion disk. Unfortunately, no similar line profile is found in other lines (e.g. H Balmer lines, He I, or He II). The absence of He II is explained through the inferred high inclination angle (an idea that is not compatible with the conclusions of this work), but the difference between the Hα and Hβ line profiles is more difficult to explain.

With increasing TDE detection rates and spectroscopic follow-up datasets, clearer evidence has emerged to associate optical emission line profiles directly with an accretion disk. Wevers et al. (2019a) and Cannizzaro et al. (2021) reported narrow Fe II emission lines likely associated with a disk chromosphere, while Holoien et al. (2019a, PS18kh), as well as Short et al. (2020) and Hung et al. (2020, AT 2018hyz), reported on flat-topped or double-peaked Hα (and other H Balmer) emission line profiles that are very likely disk-related (although see Hung et al. 2019 for an outflow scenario to explain the line profiles in PS18kh). In both PS18kh and AT 2018hyz, the inferred eccentricities are low ($\sim$0.1–0.2) and uniform, and the disk inclinations are low to moderate (20–60 degrees). This may appear somewhat surprising given the current lack of understanding of the detailed dynamics of the post-disruption debris; in particular from a theoretical point of view, it is unclear how the stellar debris can shed its (expected) large amount of energy in such a short timescale to form a quasi-circular disk (e.g. Krolik et al. 2020). In the absence of such a mechanism, the naive expectation is for the debris to form a highly elliptical structure. Using hydrodynamical simulations, Shiokawa et al. (2015) found that the returning debris is unlikely to settle into a compact, circular disk, but instead forms an extended eccentric accretion flow. Piran et al. (2015) elaborated upon these results by showing that this is consistent with the relatively small amount of energy released in stream self-intersection shocks, and furthermore that such an elliptical disk scenario can provide a natural explanation of the observed properties (e.g. luminosity, temperature, and line widths; see also Krolik et al. 2016; Svirski et al. 2017; Ryu et al. 2020a; Zanazzi & Ogilvie 2020).

In this work we present the analysis of photometric and spectroscopic data of a new TDE, AT2020zso. We describe the observations and their data reduction in Sect. 2. Our analysis methods and results are presented in Sect. 3, and we discuss these results and their implications for accretion disk formation in TDEs, as well as AGNs, in Sect. 4. We summarise our conclusions in Sect. 5. Figures of the full posterior distributions for all model fitting results are provided in the appendix, along with a table containing all the photometry used. We assume a flat Λ cold dark matter cosmology with $H_0 = 67.11\,\mathrm{km\,s^{-1}\,Mpc^{-1}}$, $\Omega_m = 0.32$, and $\Omega_\Lambda = 0.68$ (Planck Collaboration XVI 2014) throughout the article.

2. Observations and data reduction

AT 2020zso was first reported as a transient by the Zwicky Transient Facility (ZTF20acqoiyt, Forster et al. 2020), and also

detected by ATLAS (ATLASbfok; Smith et al. 2020) and *Gaia* (Gaia20fqa, Hodgkin et al. 2021). The host galaxy (SDSS J222217.13-071558.9) is an elliptical galaxy located at a redshift of $z = 0.0563$. A classification spectrum (Gromadzki et al. 2020) was obtained as part of the extended Public ESO Survey for Transient Objects (ePESSTO+; Smartt et al. 2015), and further spectroscopic follow-up was triggered within ePESSTO+. A detailed observing log is presented in Table 1. All phases are reported with respect to the phase of peak light (measured from the bolometric light curve) at MJD 59 184. The optical spectroscopy will be made publicly available through WISErep.

2.1. Spectroscopy

2.1.1. New Technology Telescope/EFOSC2

Low-resolution optical spectra were taken with the ESO Faint Object Spectrograph and Camera (EFOSC2) spectrograph mounted on the New Technology Telescope (NTT) at La Silla Observatory, Chile as part of the ePESSTO+ collaboration. We used the Gr#11, Gr#13, and Gr#16 grisms and a 1 or 1.5 arcsec slit width. The data reduction is performed using a dedicated pipeline (Smartt et al. 2015), which includes standard tasks such as bias-subtraction, flat-fielding, and a wavelength calibration based on arc frames and a comparison to sky emission lines. Cosmic rays are removed using the `lacos` routine (van Dokkum et al. 2012). To minimise host galaxy contamination, the source extraction was performed using an extraction aperture of 1 arcsec. For some epochs (in particular, those with slid widths >1 arcsec) the seeing was >1 arcsec, which may lead to different galaxy light contamination in these spectra. The Gr#16 observation is dominated above 7000 Å by second order contamination and is not used in our analysis. The flux calibration and extinction correction are performed using standard star observations.

2.1.2. Very Large Telescope/X-shooter

Shortly after the first EFOSC2 spectrum we triggered target-of-opportunity (ToO) observations with X-shooter, mounted on the Very Large Telescope (VLT) Unit 3 (Melipal) at Paranal Observatory, Chile. A total of four spectra were obtained using slit widths of 1.0, 0.9 and 0.9 arcsec for the UVB, visible (VIS), and near-infrared (NIR) arms, yielding a spectral resolution of $R = 5400$, $R = 8900$ and $R = 5600$, respectively. The data were taken in on-slit nodding mode. To increase the signal-to-noise ratio (S/N) of the UVB and VIS arms, we reduce these data using the X-shooter pipeline with recipes designed for stare mode observations. The NIR arm is reduced with both the stare and the nodding mode X-shooter pipeline recipes. The latter method provides a slightly better sky subtraction. Regardless of the method used, no transient emission features are found in the NIR spectra; they are shown in Fig. A.1 for completeness. For uniformity with the EFOSC2 spectra and to minimise host galaxy contamination, we adopt an extraction box with side 1 arcsec. Only for the last epoch (in which no TDE signal appears to be present) we use a 2 arcsec extraction box to boost the galaxy signal and determine the host galaxy properties. We use the molecfit software (Smette et al. 2015) to calculate atmospheric profiles and subtract telluric absorption bands in the VIS arm, which contaminate a small region redward of the Hα rest wavelength. The deep absorption band around 7300 Å is not well corrected, but does not contain any important emission lines. Figure A.1 shows the flux-calibrated X-shooter spectra.

Table 1. Observing log of spectroscopic observations.

Instrument	Grism	Date	MJD	Phase (days)	Slit width (arcsec)	Exposure time (s)	Wavelength range (Å)	R
EFOSC2	Gr#13	2020-11-17	59 170	−14	1.0	1500	3685–9315	850
X-shooter	UVB	2020-11-18	59 171	−13	1.0	1800	3000–5600	5400
	VIS				0.9	1920	5600–10 240	8900
	NIR				0.9JH	1920	10 240–24 800	5600
EFOSC2	Gr#11	2020-11-21	59 174	−10	1.0	1500	3380–7520	1150
EFOSC2	Gr#16	2020-11-21	59 174	−10	1.0	2700	6000–10 000	1100
EFOSC2	Gr#11	2020-11-23	59 176	−8	1.0	2700		
FLOYDS	red/blue	2020-11-26	59 179	−5	2.0	3600	3200–10 000	250
X-shooter	UVB	2020-11-28	59 181	−3	1.0	1200		
	VIS				0.9	1320		
	NIR				0.9JH	1320		
FLOYDS	red/blue	2020-11-29	59 182	−2	2.0	3600		
EFOSC2	Gr#11	2020-12-09	59 192	+8	1.0	2700		
X-shooter	UVB	2020-12-11	59 194	+10	1.0	1200		
	VIS				0.9	1320		
	NIR				0.9JH	1320		
EFOSC2	Gr#11	2020-12-16	59 199	+15	1.0	2700		
ALFOSC	Grism 4	2020-12-17	59 200	+16	1.0	900	3200–9600	360
EFOSC2	Gr#11	2021-05-10	59 344	+160	1.5	2700		750
X-shooter	UVB	2021-07-04	59 399	+215	1.0	2600		
	VIS				0.9	2720		
	NIR				0.9JH	2720		

Notes. The phase is given with respect to the peak of the bolometric light curve, taken to be MJD 59 184. The FWHM spectral resolution, R, is given at 4700 Å for EFOSC2, FLOYDS, and ALFOSC.

2.1.3. Las Cumbres Observatory/FLOYDS

Two spectra were obtained with the low-resolution FLOYDS spectrograph mounted on the Las Cumbres Observatory 2m Faulkes Telescope North in Haleakala, Hawaii. The spectra were reduced using the `floydsspec` custom pipeline, which performs flux and wavelength calibration, cosmic-ray removal, and spectrum extraction[1].

2.1.4. Nordic Optical Telescope/ALFOSC

One epoch of spectroscopy was obtained using a ToO program on the Nordic Optical Telescope (NOT) in La Palma, Spain. This spectrum was taken with the Alhambra Faint Object Spectrograph and Camera (ALFOSC) spectrograph in combination with Grism 4 and a 1 arcsec slit. This observation was reduced using custom scripts based on the pypeit Python package (Prochaska et al. 2020b,a).

Following the standard data reduction recipes, we normalise all spectra to the continuum by fitting low order spline functions to the spectra, excluding known host galaxy and transient emission and absorption lines such as the He II λ4686, He I λ5876, and Hα regions.

2.2. Photometry

We retrieve the public Zwicky Transient Facility (ZTF) photometry via the ZTF forced-photometry service (Masci et al. 2019). The multi-band light curves are shown in Fig. 1.

Following the spectroscopic classification, *Swift* follow-up observations were triggered. The *Swift* Ultra-violet Optical Telescope (UVOT) photometry is measured using the *uvotsource* task in HEAsoft package v6.29 using a 5 arcsec aperture. Because no X-ray source was detected in the first observations, we derive an upper limit to the X-ray flux using the online X-ray Telescope (XRT) tool[2]. Combining all observations, we find an upper limit of 1.56×10^{-3} cts s^{-1}, which translates into a flux of 4.5×10^{-14} erg cm^{-2} s^{-1}, assuming a thermal (blackbody) spectral model with a temperature of $kT = 75$ eV[3], typical for the soft X-ray emission in TDEs. This translates into a luminosity upper limit of 3.8×10^{41} erg s^{-1} in the 0.3–10 keV band, uncorrected for foreground Milky Way extinction. Assuming instead an AGN like power-law spectral model (with power-law index $\Gamma = 1.7$), this translates into an upper limit of 5.3×10^{41} erg s^{-1} in the 0.3–10 keV band, and 4.3×10^{41} erg s^{-1} in the 3–20 keV band.

2.2.1. Las Cumbres Observatory

Las Cumbres Observatory $BVgri$-band data were obtained using the Sinistro cameras on Las Cumbres 1m telescopes. Point-spread-function fitting was performed on host-subtracted images using the lcogtsnpipe pipeline (Valenti et al. 2016), which uses HOTPANTS (Becker 2015) for the subtraction, with template images obtained also at Las Cumbres after the event faded. BV-band photometry was calibrated to the Vega system using the AAVSO Photometric All-Sky Survey, then converted to the AB system using the corrections from Blanton & Roweis (2007),

---

[1] The pipeline is available at https://www.authorea.com/users/598/articles/6566/_show_article

[2] https://www.swift.ac.uk/user_objects/
[3] We used webPIMMS to simulate these values: https://heasarc.gsfc.nasa.gov/cgi-bin/Tools/w3pimms/w3pimms.pl
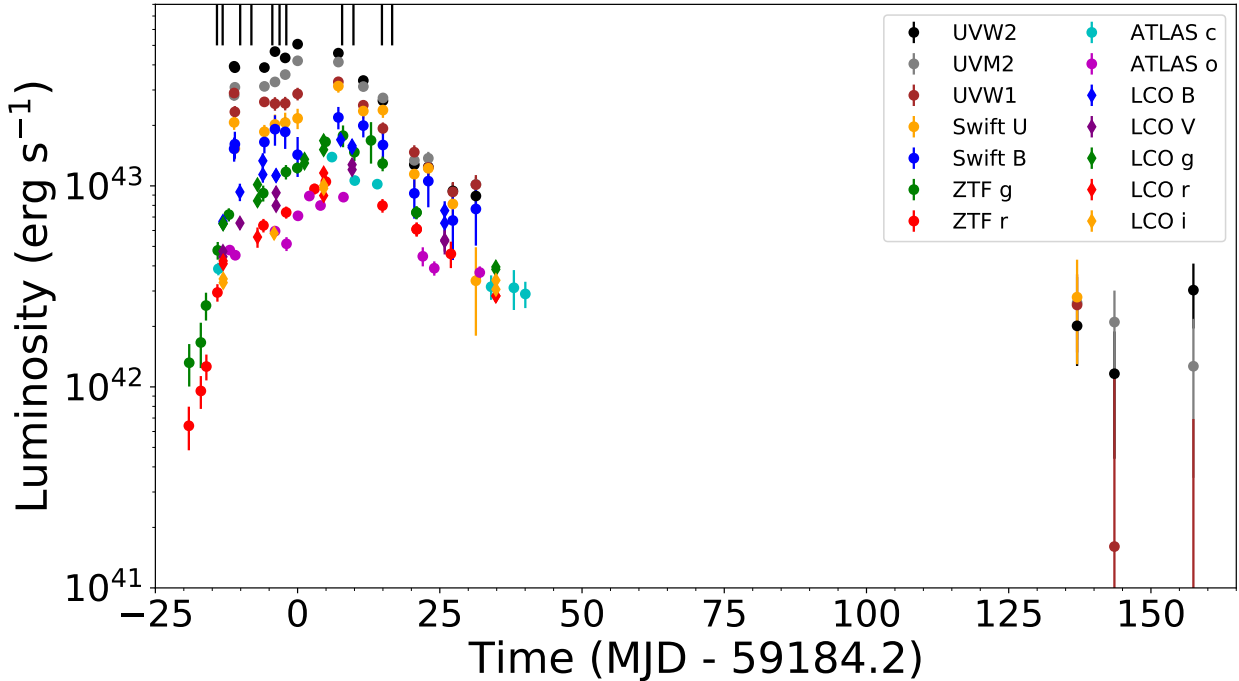
Fig. 1. Host-subtracted light curves of AT 2020zso as observed by *Swift*, ZTF, ATLAS, and LCO. Vertical lines indicate epochs of spectroscopic observations. As a result of colour evolution, the peak in the optical bands occurs significantly later than in the UV bands. This is consistent with the observed cooling of the blackbody temperature over time.

while *gri*-band photometry was calibrated to the AB system using the Sloan Digital Sky Survey (Smith et al. 2002).

2.2.2. NIR photometry

Two epochs of NIR photometry were taken on 2021 May 22 (MJD 59 356) and 2021 July 15 (MJD 59 416), at phases +172 and +232 days after peak light. The first epoch, comprising observations in the *H* (three series of six dithered 20 s exposures, for a total of 1440 s on source) and K_s (also 1440 s exposure time) bands, was taken using the Son of Isaac instrument mounted on the NTT in La Silla, Chile. The reduction and combination of dithered images were carried out with the PESSTO pipeline. The second epoch of observations, including *J*, *H* and K_s band observations, was taken with the NOTCam instrument mounted on the NOT in La Palma via the NUTS2 programme. The NOTCam data were reduced using a version of the NOT-Cam Quicklook v2.5 reduction package[4] with a few functional modifications (e.g. to increase the FOV of the reduced image).

In order to check for infrared variability, we performed aperture photometry on the NIR images. We measured the brightness of the central regions of the host galaxy with a 2 arcsec aperture and calibrated the resulting magnitude against the magnitudes of field stars taken from the Two Micron All-Sky Survey (2MASS) catalogue. The measurements were consistent within the measurement uncertainties, which were typically ~0.05 mag. We do not find any significant brightening in either epoch. Similarly, no brightening is observed in the Near-Earth Object Wide-field Infrared Survey Explorer (NEOwise) mid-infrared light curves, that is, there is no evidence for an ongoing infrared echo.

2.3. Radio observation

A weak radio detection by the Very Large Array was reported on 2020 December 21 (phase +20 days, Alexander et al. 2021). A reported flux density of 22 ± 7 micro-jansky at 15 GHz corresponds to a monochromatic luminosity of 2.73 ± 0.87 × 10^{37} erg s^{-1}.

2.4. Gaia astrometry

AT 2020zso was detected by the *Gaia* Photometric Science Alerts (GSAs; Hodgkin et al. 2021) as Gaia20fqa at coordinates (RA, Dec) = (22:22:17.130, –07:15:59.08). This allows an accurate evaluation of the positional offset with respect to the host galaxy nucleus, which has positional coordinates listed in the Early *Gaia* Data Release 3 (Gaia Collaboration 2021). An offset of 42 milli-arcseconds (mas) is measured, which corresponds to 46 parsec (pc) at the host redshift. The per-transit accuracy of GSAs is 55 mas (Wevers et al. 2019a; Hodgkin et al. 2021), leading to an offset of 46 ± 60 pc, consistent with a location in the nucleus of the galaxy.

3. Analysis and results

3.1. Host galaxy

3.1.1. Spectral energy distribution

We compiled the host galaxy (SDSS J222217.13-071558.9) spectral energy distribution (SED) using archival observations in the UV through infrared bands (see Table 2 and Fig. 2). In the NIR we used 2MASS (Cutri et al. 2003) *J*, *H*, and K_s magnitudes, and we used the Pan-STARRS DR1 magnitudes in *g*, *r*, *i*, *y*, and *z* optical bands. Finally, for the UV we performed aperture photometry in the Galaxy Evolution Explorer (GALEX; Bianchi et al. 2011) *NUV* and *FUV* images with the

Table 2. Results of the host SED model fitting of the 5″ aperture data.

Band	Observed (AB mag)	Model (AB mag)
GALEX *FUV*	20.97 (0.23)	21.04 (0.10)
GALEX *NUV*	20.24 (0.10)	20.50 (0.10)
PS1 *g*	17.93 (0.02)	17.87 (0.01)
PS1 *r*	17.29 (0.01)	17.29 (0.01)
PS1 *i*	16.96 (0.01)	16.97 (0.01)
PS1 *y*	16.67 (0.04)	16.66 (0.01)
PS1 *z*	16.81 (0.01)	16.77 (0.01)
2MASS *J*	16.10 (0.08)	16.47 (0.02)
2MASS *H*	16.48 (0.16)	16.31 (0.02)
2MASS K_s	16.15 (0.11)	16.52 (0.03)
UVOT *U*	–	19.42 (0.04)
UVOT *B*	–	18.26 (0.02)
UVOT *V*	–	17.58 (0.01)
UVOT *UVW2*	–	20.62 (0.09)
UVOT *UVM2*	–	20.52 (0.10)
UVOT *UVW1*	–	20.23 (0.08)

Notes. Values between brackets indicate the uncertainties, which are propagated into the host-subtracted photometry.

Fig. 2. Host galaxy SED and best-fit template used to synthesise host galaxy magnitudes in the *Swift* bands. The data are tabulated in Table 2.

gPhoton package (Million et al. 2016). We performed forced aperture photometry in all available bands with two distinct apertures. For one set, we used 5 arcsec apertures; this was used to subtract the host contribution from the observed light curves (in particular, the *Swift* photometry is performed with a 5″ aperture). For the other set, we used an elliptical aperture with major and minor axes of 13 and 9 arcsec, optimised to include the entire host galaxy flux; this was used to model the host galaxy and derive its properties.

We modelled the SED using the flexible stellar population synthesis (Conroy et al. 2009) module. We used the Prospector (Johnson et al. 2021) software to run a Markov chain Monte Carlo (MCMC) sampler (Foreman-Mackey et al. 2013). We assume an exponentially decaying star formation history (SFH), and a flat prior on the five free model parameters: stellar mass ($M_\star$), stellar metallicity (Z), V-band extinction (A_V, assuming the extinction law from Calzetti et al. 2000), the stellar population age (t), and the e-folding time of the exponential decay of the SFH (τ_{sfh}).

Using the median and 1-σ confidence intervals of the posteriors of the fit to the 9″ by 13″ aperture photometry, we derive a host stellar mass of $\log(M_\star/M_\odot) = 10.11^{+0.02}_{-0.02}$, a metallicity of $\log(Z/Z_\odot) = -0.34^{+0.04}_{-0.07}$, $A_V = 0.23^{+0.03}_{-0.04}$ mag, $t = 1.90^{+1.56}_{-0.94}$ Gyr, and $\log(\tau_{sfh}) = 2.42^{+0.35}_{-0.32}$ Gyr. The extinction is roughly consistent with the Galactic foreground extinction of $E(B - V) = 0.06$ (Schlafly & Finkbeiner 2011). The estimated mass combined with the extinction-corrected rest-frame colour $u - r = 1.89 \pm 0.02$ mag places the host galaxy near the 'green valley' region (Schawinski et al. 2014) of the mass colour diagram, in which the TDE host galaxies seems to be over represented compared to the general galaxy population (Law-Smith et al. 2017; van Velzen et al. 2021; Hammerstein et al. 2021).

To estimate the host galaxy fluxes in the UVOT bands, we similarly model the host galaxy SED but using the 5″ aperture data. The host contribution is then subtracted from the measured photometry, which is also corrected for foreground Galactic extinction. The uncertainty on the host galaxy model is propagated into our measurement of the host-subtracted TDE flux (see Table 2).
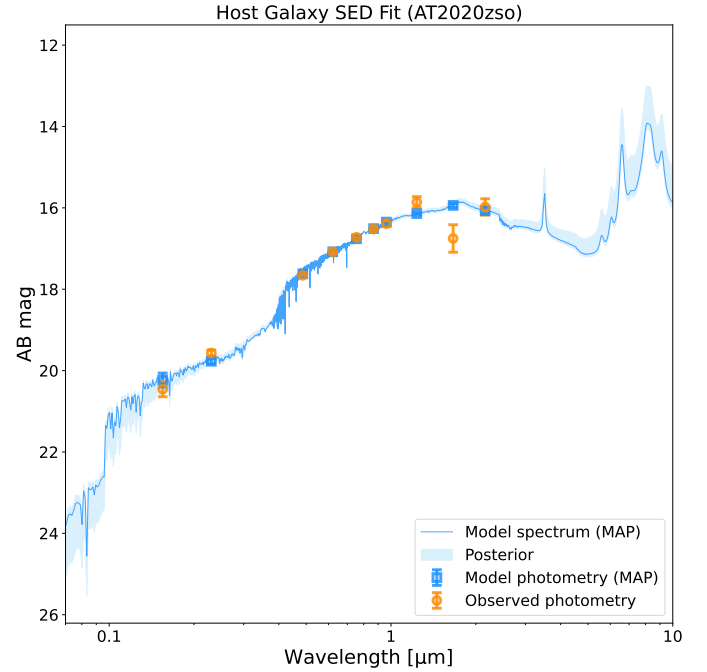
3.1.2. Black hole mass

Using the late time X-shooter spectrum, in which no broad emission lines are apparent, we measure the velocity dispersion of the host galaxy following the method of Wevers et al. (2017), using the penalised pixel fitting routine (Cappellari 2017). We find a velocity dispersion of $\sigma = 60 \pm 1\,\mathrm{km\,s^{-1}}$. Using the $M - \sigma$ relation from McConnell & Ma (2013) this translates to a black hole mass of $\log(M_{BH}) = 5.3 \pm 0.4$, or alternatively $\log(M_{BH}) = 6.2 \pm 0.3\,M_\odot$ using the Kormendy & Ho (2013) relation, indicating a low mass black hole similar to many other UV/optical discovered TDEs (Wevers et al. 2019b).

3.1.3. Emission lines

From the narrow host galaxy emission lines, which are resolved in the X-shooter spectra, we measure a redshift of $z = 0.0563$, which corresponds to a luminosity distance of 263 Mpc.

We identify a plethora of narrow emission lines originating in the host galaxy, including in order of increasing wavelength: the [O II] $\lambda\lambda 3726, 3729$ doublet, [Ne III] $\lambda 3869$, He II $\lambda 4686$, Hβ, the [O III] $\lambda\lambda 4959, 5007$ doublet, He I $\lambda 5876$, [O I] $\lambda 6300$ line, the [N II] $\lambda\lambda 6548, 6584$ doublet, Hα, the [S II] $\lambda\lambda 6717, 6731$ doublet, a (very) weak [Ar III] $\lambda 7136$ line, the [S III] $\lambda\lambda 9069, 9532$ doublet lines, and Pa α $\lambda 1.875\,\mu$m. High-ionisation-potential lines such as He II, [Ar III] and [S III] indicate that a hard photoionising continuum source is present, while there is no sign of a broad component to any of these lines at late times. We measure a full width at half maximum (FWHM) from the [O III] line of $159 \pm 3\,\mathrm{km\,s^{-1}}$, while for the narrow H$\alpha$, H$\beta$, N II, and S II lines we measure an average of $FWHM = 127 \pm 5\,\mathrm{km\,s^{-1}}$. Closer inspection shows that some of these narrow lines are asymmetric/double-peaked, with a velocity separation of $\sim 70 - 80\,\mathrm{km\,s^{-1}}$. Figure 3 shows some of the prominent narrow emission line profiles. We measure the asymmetry of the [O III]
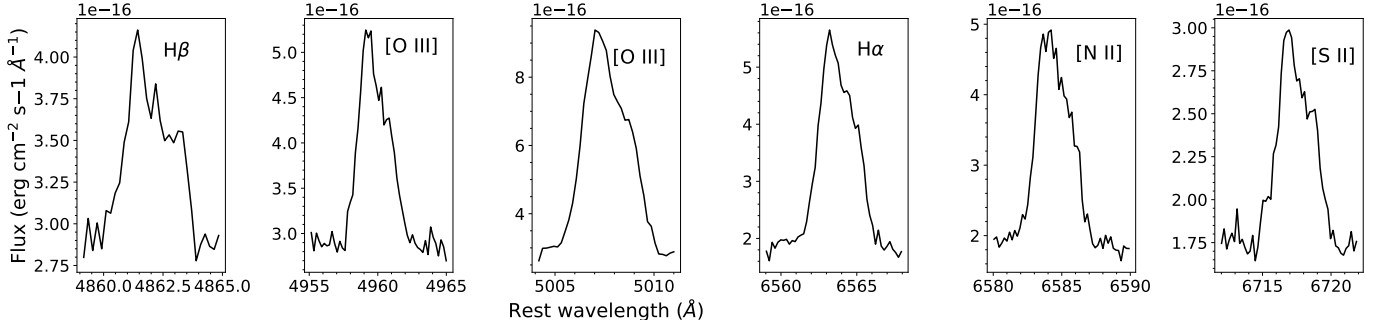
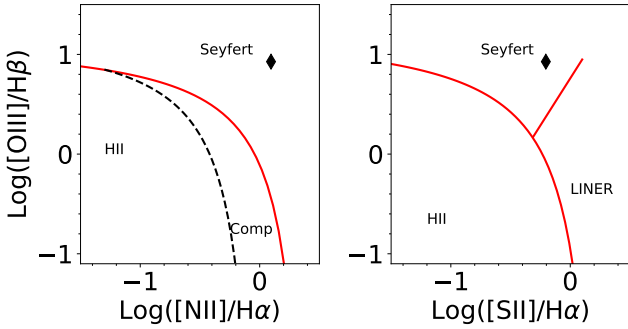**Fig. 3.** Insets of the narrow emission lines observed in AT2020zso.

Fig. 4. Narrow emission line ratios as measured from the late-time X-shooter spectrum. The results place the host galaxy firmly into the AGN (Seyfert) part of the diagram. Dividing lines are taken from Kewley et al. (2001) and (2006).

Fig. 5. MOSFit model light curves overlaid on the data. The fits are not great, likely due to the relatively rapid temperature evolution and peculiar light curve behaviour (including a break in the rising part), which the model cannot accommodate.

$\lambda 5007$ line, the strongest narrow emission line, by using the non-parametric measurement of Liu et al. (2013), and find a very small asymmetry $A = 0.047$ (other lines yield similar values). This suggests that the narrow line region is rotation dominated, but probably not kinematically disturbed (Blecha et al. 2013; Nevin et al. 2016), which makes it very unlikely that the system hosts a dual AGN or a wide-separation SMBH binary. We measure an [O III] line luminosity from the late time spectrum of $L_{\rm [OIII]} = 1.17 \pm 0.05 \times 10^{40}$ erg s^{-1}. Assuming a correlation between $L_{\rm [OIII]}$ and the 3–20 keV X-ray luminosity observed in AGNs (Heckman et al. 2005), we expect an AGN X-ray luminosity of $L_X = 1.6 \times 10^{42}$ erg s^{-1}. The upper limit for L_X derived from *Swift* observations is 4.3×10^{41} erg s^{-1} in the 3–20 keV band, which is marginally inconsistent given the large scatter (a factor of ≈ 3) in the correlation. Reconciling these two values (again assuming a power-law spectrum with index $\Gamma = 1.7$) would require an absorbing column of at least ~ 1–1.5×10^{22} cm^{-2}.

We also use the narrow host galaxy line ratios to put the source on a Baldwin-Philips-Terlevic (BPT) diagram (Baldwin et al. 1981). We find that the source falls well into the AGN/Seyfert part of the diagram, in line with the presence of high-ionisation narrow emission lines (Fig. 4). We conclude that this galaxy hosts a Seyfert AGN.

3.2. Light curve evolution

The host-subtracted light curves are shown in Fig. 1. The best sampling is achieved in the ZTF bands, particularly at very early times. There appear to be three distinct phases in both the g- and r-band light curves: a very steep initial rise, followed by a
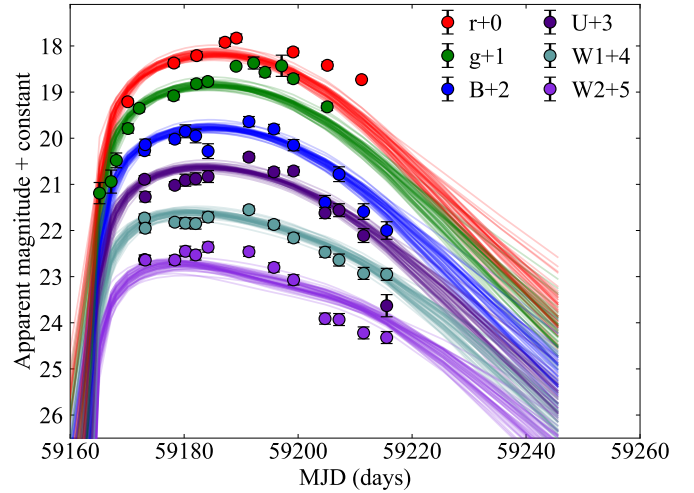
break to a slower increase in brightness and finally a turnover to a decline in brightness. To characterise the light curve behaviour at early times, we fit a power-law model to the two parts of the rising ZTF light curve (before and after the break) independently, of the form

$$L = a + b \times (t - t_0)^{\alpha}. \tag{1}$$

We find that the early rising part of the light curve is consistent with $L \propto t^2$ evolution ($\alpha = 1.9 \pm 0.4$). After the break (which happens around phase $= -12$ days), the slope flattens to $\alpha = 1.55 \pm 0.25$. We remark that the emission lines contribute $<10\%$ of the total light, and therefore do not significantly influence the light curve evolution nor the inferred parameters.

3.2.1. Parameter inference with MOSFit and TDEMASS

We fit the light curve using a TDE model in the MOSFit package (Guillochon et al. 2018; Mockler et al. 2019), employing the same free parameters and priors as in Mockler et al. (2019). We used the DYNESTY dynamic nested sampling algorithm with default stopping criteria to explore the parameter space and sample the model posteriors (see Speagle 2020, for details). The MOSFit TDE model only includes the fallback luminosity as an energy source, while at later times $\gtrsim 100$ days (e.g. Mummery & Balbus 2020a) there may be a significant contribution from an accretion disk, leading to a flattening of the light

Table 3. Results of the light curve fitting with MOSFit (16–84 percentiles).

Parameter	Value
$\log_{10}(M_{\rm BH})$ ($M_\odot$)	5.9–6.1 [0.2]
Stellar mass ($M_\odot$)	0.08–0.13 [0.36]
Impact parameter β	0.58–0.68 [0.35]
ϵ	0.05–0.13
$\log_{10}(R_{\rm pho})$	2.65–3.31
Photospheric exponent l	3.45–3.91
$\log_{10}(T_{\rm visc})$ (days)	–1–0.82
$t_{\rm expl}$ (days)	–10.2–5
$\log_{10}(\sigma)$	–0.47–0.39

Notes. The systematic uncertainties are taken from Mockler et al. (2019) and provided in square brackets, when available.

curve. We therefore exclude data points more than 100 days after peak luminosity from the fit, while noting that a fit including these data does not significantly alter the black hole mass and stellar mass estimates. Fits were run on the University of Birmingham BlueBEAR cluster.

The results are a poor fit (Fig. 5); there are short-term variations that are not encapsulated by the model itself, so these are not expected to be reproduced, and the temperature variation is more rapid than the model can accommodate. These results should therefore be interpreted with some caution.

A black hole mass of $\log_{10}(M_{\rm BH}) = 6.0 \pm 0.3$ is inferred from the light curve, which is consistent with the estimate from the stellar velocity dispersion. Furthermore, we obtain estimates of the disrupted stellar mass (at the lower allowed limit of $\sim$0.1 $M_\odot$) and the impact parameter $\beta \equiv \frac{R_{\rm p}}{R_{\rm t}} = 0.63 \pm 0.05$ (where $R_{\rm p}$ is the orbital pericentre radius, and $R_{\rm t}$ the tidal radius), although there are large systematic uncertainties of 0.66 dex or 0.36 in a linear scale for a value of 0.1 for the stellar mass, and 0.35 for the impact parameter (see Mockler et al. 2019 for a detailed discussion of the systematic uncertainties produced by MOSFit). The results of these fits are reported in Table 3, and full posterior distributions for the fits can be found in the Appendix. These values are very similar to those found by Gomez et al. (2020) for the other double-peaked TDE AT 2018hyz, and indicate that AT 2020zso may likewise be the result of a partial, rather than a full, disruption (as inferred from the fact that $\beta < 0.9$; e.g. Guillochon & Ramirez-Ruiz 2013). Simulations by Ryu et al. (2020b) suggest that the surviving stellar remnant may have lost $\sim$40 per cent of its original mass (but keeping in mind the large systematic uncertainties, this could range from a few up to >60 per cent). Finally, MOSFit suggests a disruption date of 8 ± 2 days before the first data point, at MJD 59 157 ± 2 days.

Alternatively, Ryu et al. (2020a) presented a framework to infer the black hole and disrupted stellar masses on the basis of eccentric accretion disk dynamics. Using the peak bolometric luminosity of $7 \pm 1 \times 10^{43}$ erg s^{-1} and a peak colour temperature of 25 000 $\pm$ 5000 K, a black hole mass of $M_{\rm BH} = 1.7^{+2.0}_{-0.9} \times 10^6$ $M_\odot$ and stellar mass of $M_\star = 0.92^{+0.21}_{-0.13}$ $M_\odot$ are inferred; the former is consistent with alternative estimates from galaxy scaling relations, while the latter differs significantly from the MOSFit estimate. Given that the TDEMASS framework was explicitly developed on the basis of eccentric accretion disk dynamics, which appear to be particularly suited for application to AT2020zso, we give preference to these inferences.

3.2.2. Blackbody modelling

The properties of UV/optical TDE flare emission can be empirically be well described using evolving blackbody models. This is somewhat surprising, given that there is growing evidence for a viewing angle dependence of the observational consequence of stellar destruction (Dai et al. 2018; Leloudas et al. 2019), implying that asymmetry is present in the ensuing structure. As a result, it is unclear to what degree the results of blackbody fitting the TDE SED can be physically interpreted.

With this caveat in mind, for each epoch of *Swift* observations, we model the SED using a blackbody curve, although the physical interpretation of this model is unlikely to be straightforward, as the powering source of this emission remains unclear. We include all the host-subtracted *Swift* photometry, and linearly interpolate the ZTF g- and r-band measurements to these epochs to provide coverage from 2000–7000 Å. We do not extrapolate the ZTF measurements beyond their latest observing epochs. We use a maximum likelihood approach to fit a blackbody model to each epoch, assuming a flat prior for all parameters; the resulting fits are illustrated in Fig. 6. Uncertainties are assessed by sampling from the posterior distributions of the parameters directly. Assuming isotropic emission also yields the characteristic blackbody radius. The temperature, radius and bolometric blackbody luminosity are shown in Fig. 7; the values based only on ZTF (without temperature fit, but with a bolometric correction) data are shown as green triangles.

The temperature decreases by $\sim$10 000 K during the first part of the light curve. Several sources in the van Velzen et al. (2021) sample show similar behaviour. Such cooling is typically seen in TDEs after peak, likely as a result of an expanding photosphere, although the effect is particularly strong for AT 2020zso (a similar effect was seen in AT2019qiz; Nicholl et al. 2020). The MOSFit results show a similar temperature evolution, although the temperature changes somewhat slower (this is intrinsic to the TDE model). There is some indication of an increasing trend at later times (again similar to typical TDE behaviour), but the uncertainties are large.

The photosphere radius evolution follows a linear expansion profile initially. We measure an expansion velocity of $v_{\rm exp} = 2900 \pm 300$ km s^{-1} before peak light (Fig. 8, top panel). Afterwards, the radius reaches a plateau before moving back inwards to scales $\approx 5 \times 10^{13}$ cm. This behaviour is very similar to that observed in AT2019qiz (Nicholl et al. 2020) and AT2019ahk (Holoien et al. 2019b). Based on the expansion velocity before maximum, we estimate that the first observations were taken approximately 15 days after expansion began, suggesting a disruption date around MJD 59 149, and a rise time of approximately 35 days from disruption to peak (compared with an explosion date of MJD 59 157 from MOSFit). This value is insensitive to the assumption about the temperature evolution before the first *Swift* observations.

We note that an expanding photosphere does not necessarily require a physical outflow (i.e. outward fluid motion) to be present. Alternatives to explain the photosphere expansion include the accumulation of matter around the peak of the mass fallback rate, which extends the photosphere to larger radii; it could be the result of time-dependent photon diffusion due to changing density and/or optical depth in the debris; or due to the orbital motion of heated matter, which at the inferred radius of $\sim$5 $\times 10^{14}$ cm is comparable ($\sim$5000 km s^{-1}) to the measured growth rate.
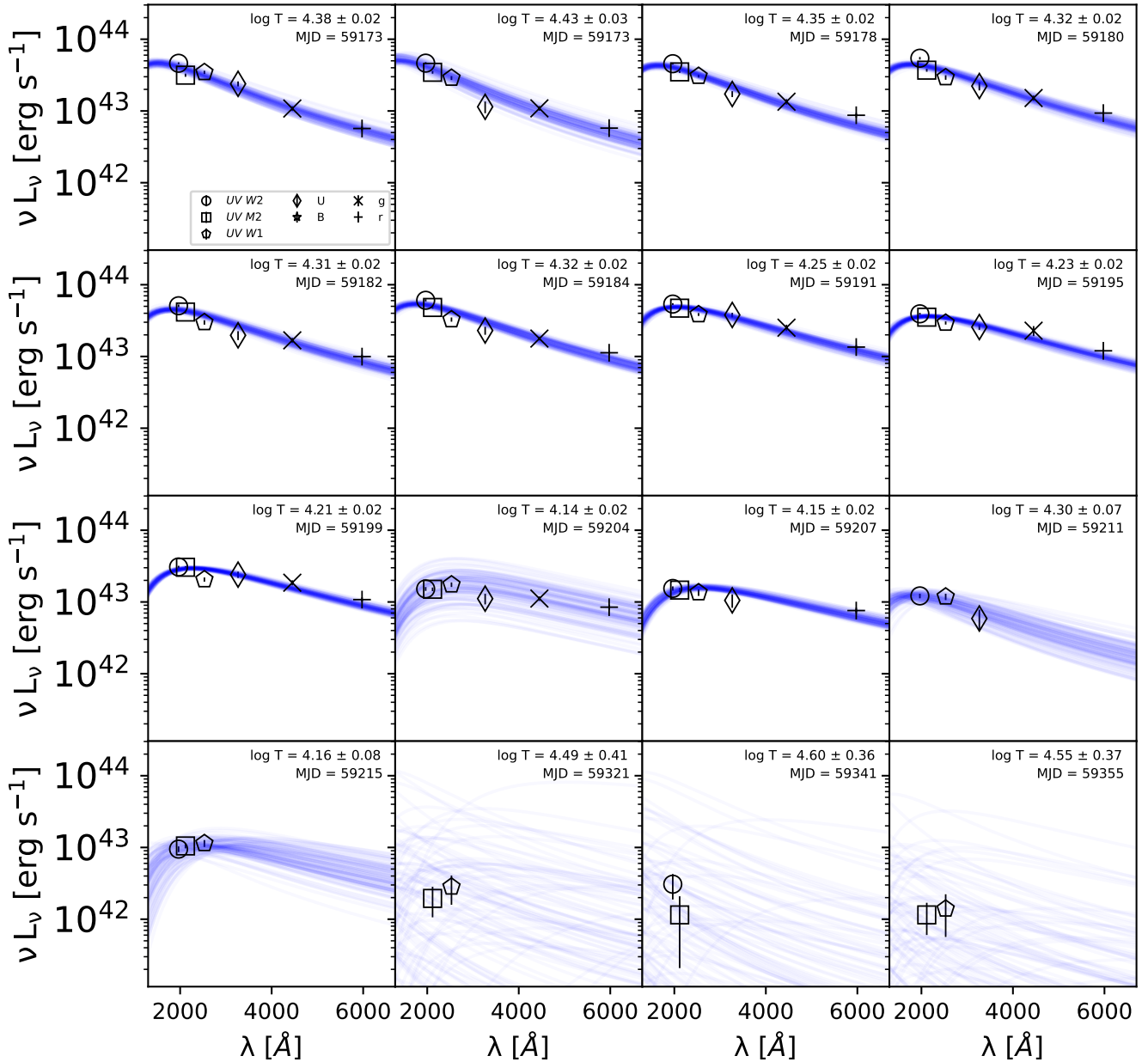
Fig. 6. Blackbody fitting of the TDE SED over time. The uncertainties become very large for the last three epochs as two data points do not provide much constraining power for the blackbody model.

3.3. Transient emission features

In addition to the narrow host galaxy lines, broad evolving emission lines are present in the spectra, which are shown in Figs. 9 and 10. These lines are typically (quasi-)Gaussian in TDEs, with velocity shifts up to ~15 000 km s^{-1}. However, in AT 2020zso there are several emission features whose identification would be contrived, or completely unclear, when taking this approach. For example, a broad feature centred on 4500 Å appears around −4 d. While this could in principle be broad Fe II emission often seen in AGNs, the profile appears smooth with a broad blue wing that would be atypical. Similarly, broad features centred on 4250 Å, 5050 Å, 6080 Å, and 6820 Å are present in several of the spectra. No similar features have been readily identified in other TDEs to date, and no immediately obvious line identifications are available for these wavelengths.

Noting that these broad emission features appear to be roughly symmetrical around rest wavelengths of ~4700 Å and 6560 Å, we instead explored the idea that these are multi-peaked structures constituting a single feature, that is, emission lines of He II/Hβ and Hα. This is motivated by previous studies that have identified double-peaked emission lines, attributed to accretion disk structures, in TDEs (Arcavi et al. 2014; Short et al. 2020; Hung et al. 2020).

The velocity structure of these lines is shown in Fig. 11; it is encouraging that the profiles appear very similar in this representation. We identify the emission features with two main contributors, consistent with rest wavelengths of He II λ4686 and Hα. Because Hα appears centred near rest velocity, we disfavour an identification as Hβ for the emission feature near 4700 Å; such an identification would require a large systematic blueshift (−11 000 km s^{-1}), whereas for He II the line would also be
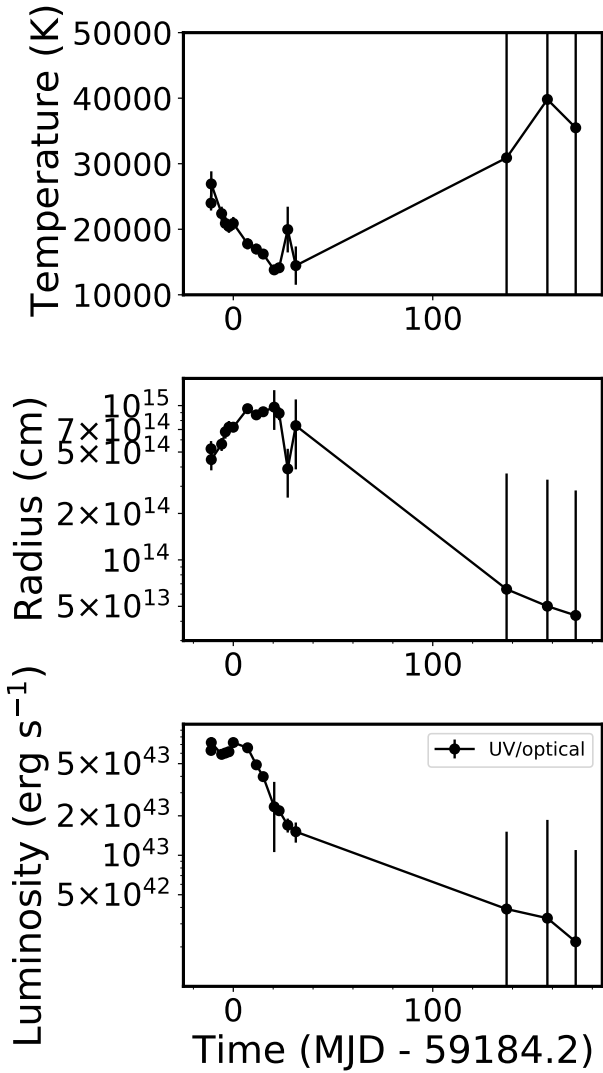
Fig. 7. Blackbody parameter evolution of AT2020zso over time. Strong cooling is observed during the first part of the light curve.

centred near rest velocity. Nevertheless, the broad feature around 5050 Å may identify as the red wing of a similar double-peaked velocity profile consistent with Hβ, albeit much weaker than He $\text{\textsc{ii}}$. No other broad He $\text{\textsc{ii}}$ emission lines (e.g. at $\lambda\lambda3203, 10\,123$ Å) are evident in the spectra. We also note that there are other emission features seen in TDEs around this region, most notably the Bowen N $\text{\textsc{iii}}$ 4640 line. We explore possible contamination in more detail in Sect. 3.5.

Given the strongly non-Gaussian line profiles, we measure the emission line equivalent widths (EWs) of the He $\text{\textsc{ii}}$ complex and Hα through direct integration. We mask out telluric absorption features in the spectra when present. The EW evolution and their ratio is shown in Fig. 12. The He $\text{\textsc{ii}}$/Hα ratio decreases rapidly from ≈11 (phase -14 days), to 7 (phase -13 days), to stabilise around 1.5 (phases later than -10 days). For the earliest epochs, we also measure the EW ratio by using a Gaussian profile, which yields somewhat lower values (≈8 and 4 at -14 and -13 d, respectively) but shows a consistent, rapidly decreasing trend.

The first four epochs are well described (reduced $\chi^2 < 1.3$) by a broad, single Gaussian, and for these spectra we also attempt to measure the line velocities and FWHM of He $\text{\textsc{ii}}$ and
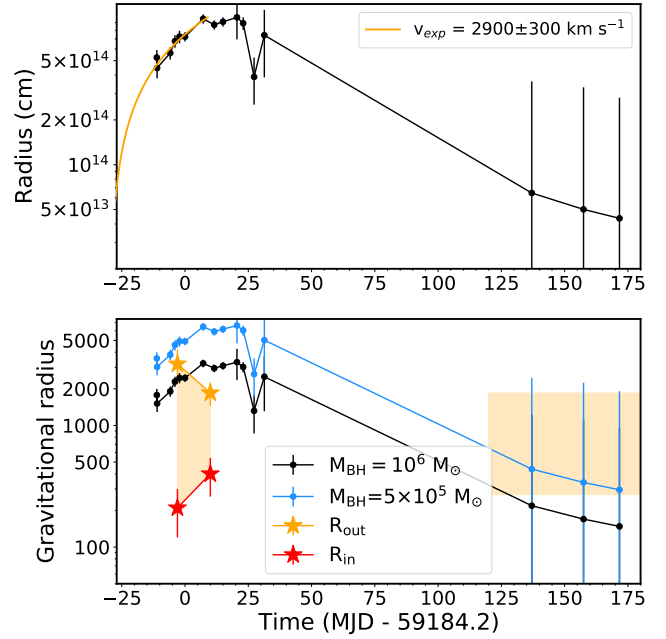

Fig. 8. Blackbody radius evolution over time. *Top panel*: evolution of the blackbody radius, overlaid with the best-fit linear expansion model (orange line). At late times the radius reaches approximately 5×10^{13} cm (but with large error bars), which corresponds to several hundred R_g for $M_\text{BH} = 10^6 M_\odot$. *Bottom panel*: same evolution, but now converted to units of gravitational radius for two different black hole masses. The orange and red stars mark the inferred disk outer and inner radii, respectively (see Sect. 3.6). At late times, the blackbody radii overlap with the estimated accretion disk size (highlighted with the shaded area, assuming that the disk size has not changed significantly from the last epoch that can be modelled).

Hα. The results indicate that both lines are likely at rest velocity. All measurements are consistent with 0 within 3σ, although we find large variations between different spectra that are unphysical given that they were taken only days apart, likely due to the relatively low S/N. The 'best' early spectrum available was taken with X-shooter (phase -13 days), from which we measure line velocities of 800 ± 400 km s^{-1} and -170 ± 135 km s^{-1} for Hα and He $\text{\textsc{ii}}$, respectively. From the same spectrum, we measure Gaussian FWHM values of $36\,000 \pm 7000$ (Hα) and $31\,000 \pm 1000$ (He $\text{\textsc{ii}}$) km s^{-1} (for a reduced χ^2 of 1.2).

3.4. Emission line evolution

We plot the broad emission line profiles of He $\text{\textsc{ii}}$ and Hα in Fig. 11. For clarity, we focus on the highest spectral resolution (X-shooter) spectra. We start by noting that there appears to be a delay between the emergence of He $\text{\textsc{ii}}$ (which appears earlier) and Hα, which is very weak in the earliest epochs but strengthens ~10 days after the first observation (as is also apparent from the EW evolution in Fig. 12). The line profile of He $\text{\textsc{ii}}$ is slightly asymmetric and peaks around -3000 km s^{-1}, which would be consistent with the photospheric outflow velocity measured through blackbody modelling.

Near peak light (phase -3 days) the spectra become distinctly non-Gaussian. The He $\text{\textsc{ii}}$ line profile is inconsistent with the presence of a very broad Gaussian (similar to the one observed at -13 days) – this component would extend well beyond 4300 Å, where no excess flux is observed. Both lines show a double-peaked structure, centred near rest wavelength; He $\text{\textsc{ii}}$
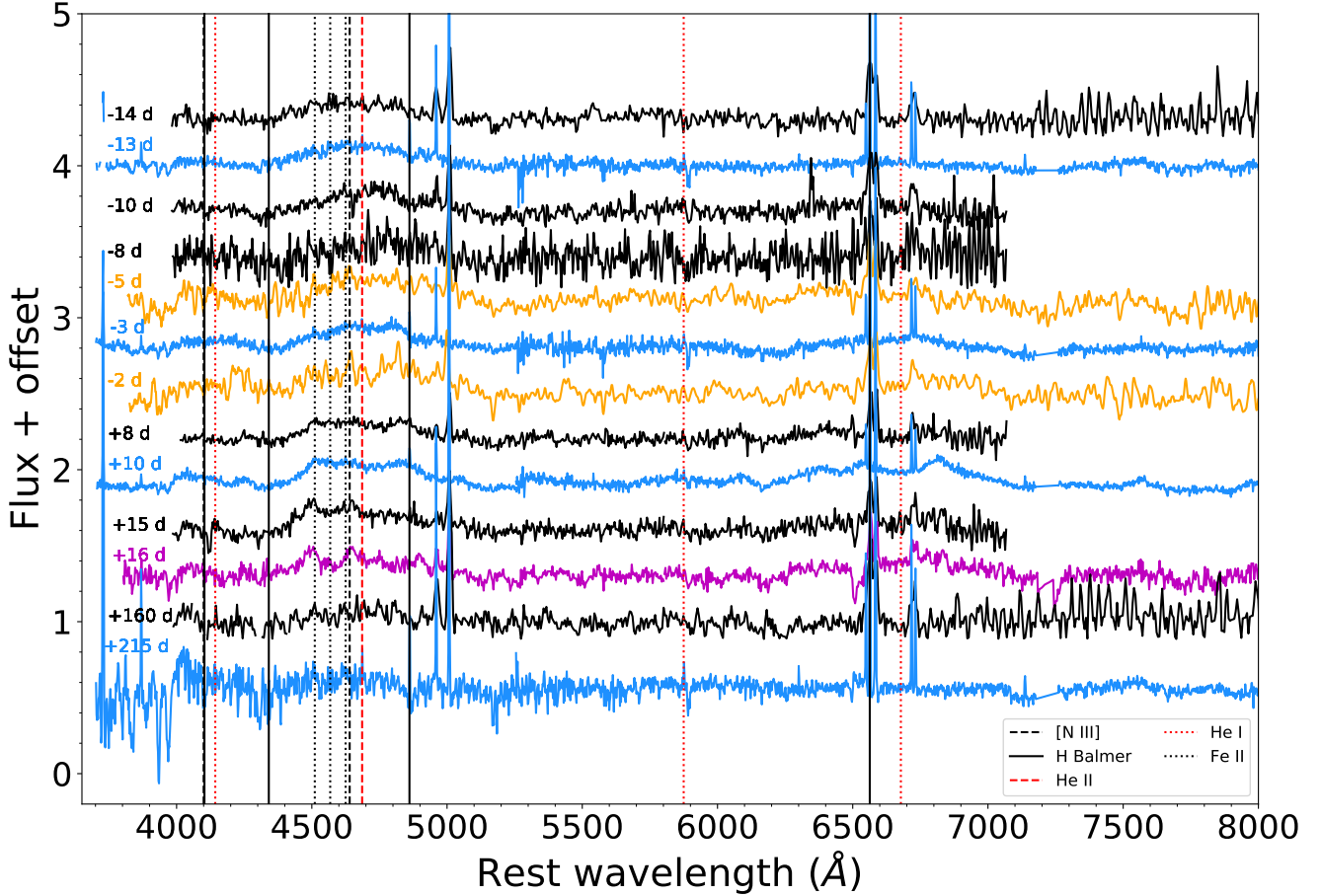
Fig. 9. Spectral evolution of AT 2020zso from early to late times. All spectra are continuum normalised. The different emission features in the 4600 Å blend are indicated with vertical lines: solid black lines indicate H Balmer lines, dashed black lines N III, dotted black lines Fe II, red dashed lines He II, and red dotted lines He I. Black spectra were taken with NTT/EFOSC2, blue with VLTX-shooter, orange with LCO/FLOYDS, and magenta with NOT/ALFOSC. The X-shooter spectra are resampled at lower spectral resolution for clarity. The gap around 5200 Å is due to the low S/N of the data at the edges of the UVB and VIS arms, and the gap around 7300 Å is due to the poor correction of molecular bands.
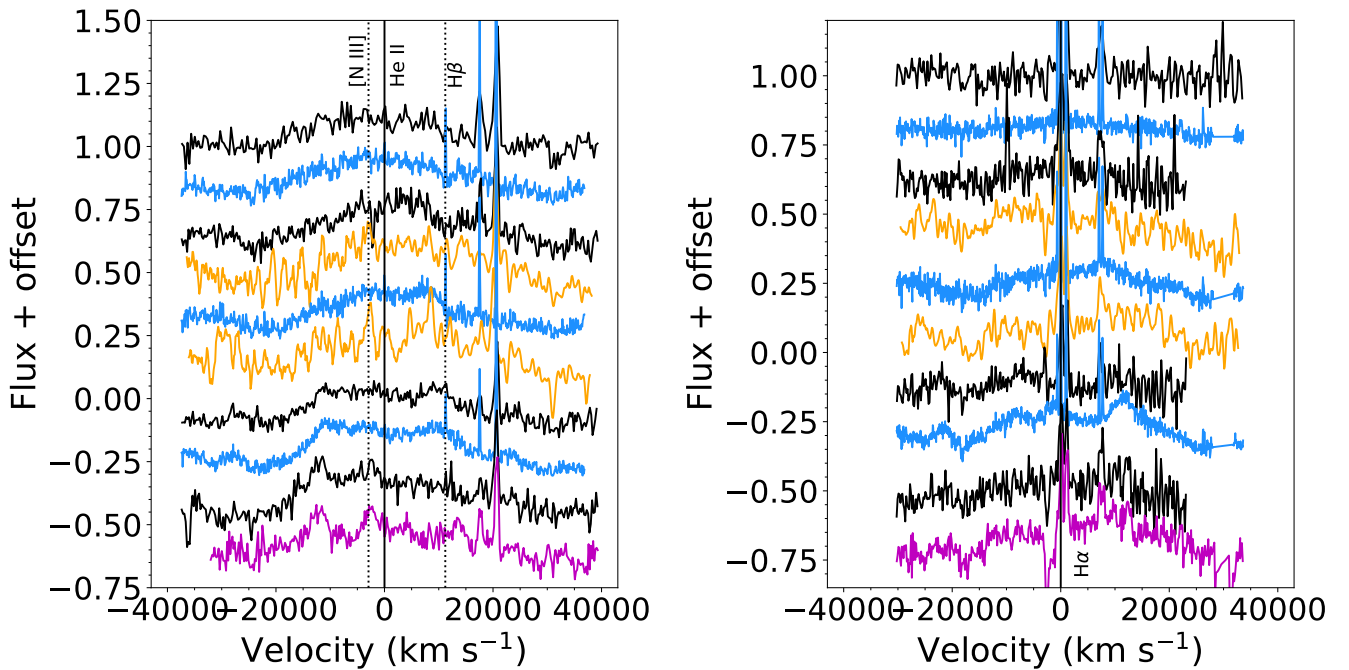

Fig. 10. Same as Fig. 9, but now in velocity space. *Left panel*: the He II region, and the *right panel* shows the region around Hα.
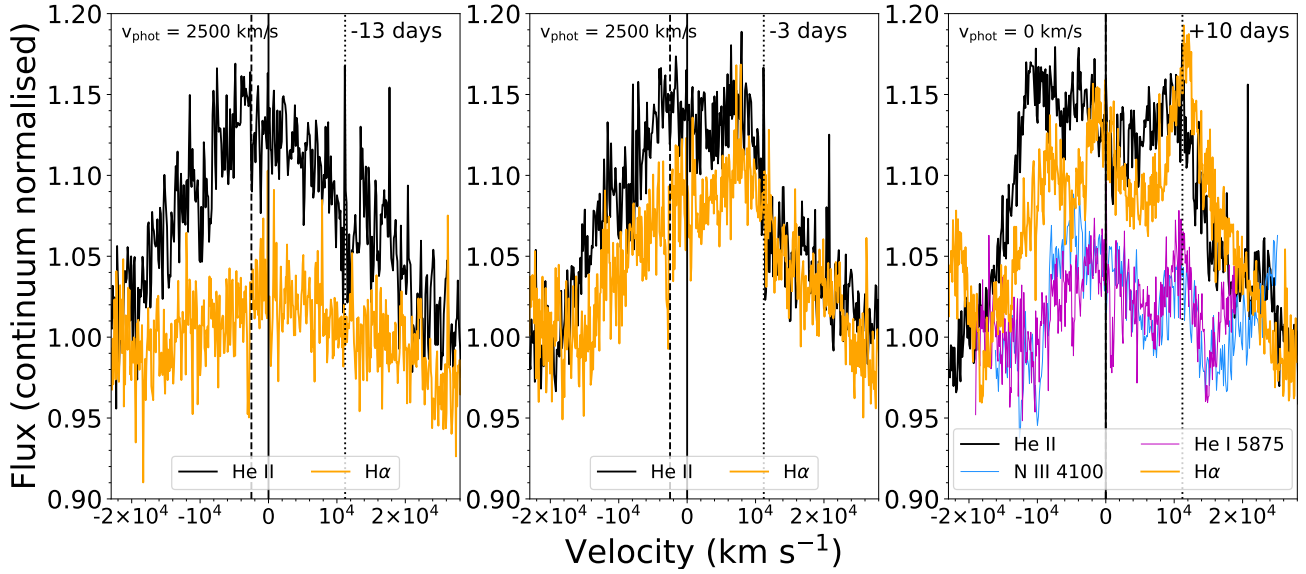
Fig. 11. VLT/X-shooter spectra at various epochs, plotted in velocity space for He II (black) and Hα (orange). To guide the eye, we show: the rest velocity as a solid line; the photospheric velocity with a vertical dashed line, which happens to coincide with the expected position for N III $\lambda4640$; and the position for Hβ with respect to He II as a black dotted line. For display purposes, narrow emission lines have been removed and the spectra are resampled to lower spectral resolution.
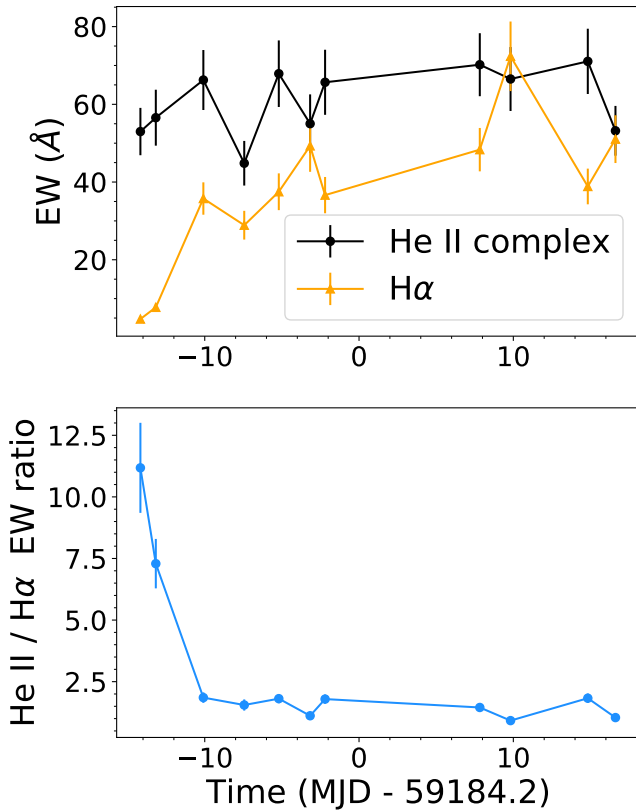

Fig. 12. Emission line measurements and their evolution over time. *Top panel*: equivalent width of the He II complex (black circles) and Hα (orange triangles), measured through direct integration from the spectra. *Bottom*: their ratio (He II/Hα) as a function of time.

appears roughly symmetric whereas Hα shows a strong asymmetry, with a bright red peak and a broad blue shoulder (no clear blue peak is visible in the spectrum). The red peak of both lines occurs at similar velocities ($\sim$8000 km s^{-1}), and the

red wing is nearly identical in velocity structure, extending out to $\approx$26 000 km s^{-1}. On the blue side, the He II profile extends roughly 5000 km s^{-1} further blueward (out to 18 000 km s^{-1}) compared to Hα, and is a factor of $\sim$2 brighter than Hα. This could indicate either that the He II emission originates from a region with a different velocity profile or potential contamination of other emission lines known to be present in this region (including N III $\lambda4640$ and Fe II lines), discussed in Sect. 3.5.

After peak light (phase +10 days), the profiles have significantly evolved. Hα shows a pronounced triple-peaked structure. In particular the red peak of the profile is remarkable, being significantly brighter and more narrowly peaked than its blue equivalent. Similar to the previous epoch, the red wings of Hα and He II have comparable velocity structures. However, the red peak has moved to higher velocities, particularly for Hα ($\sim$11 500 km s^{-1}). He II remains broader and brighter in the blue wing, extending out to 21 000 km s^{-1}. The blue Hα peak is situated around $-$8000 km s^{-1}, whereas He II peaks closer to $-$10 000 km s^{-1}. The 'central' peak of Hα is more pronounced and near rest velocity.

We note that the photospheric radius has reached a plateau at this phase (+10 d), that is, the outflowing photosphere reaches its maximum radius before becoming optically thin and receding inwards. The origin of these central features could therefore be either from the accretion disk itself[5] or (less likely) in this outflowing component near maximum radius, consistent with the low observed velocities.

It is worth noting that there is no pronounced central peak in He II, although some feature may be present. This is unlikely to be the blue wing of a double-peaked Hβ line profile, because (i) this would imply a velocity of $-$14 000 km s^{-1}, significantly larger than both the Hα and He II blue peak velocities, and (ii) for Hα the red peak is brighter than the blue peak, whereas such an identification would imply a stronger blue peak for Hβ. Alternatively, this feature could be consistent with Bowen N III $\lambda4640$.

---

[5] See Fig. A.2 in the Appendix for an example of how large eccentricities lead to this third middle bump.

This remarkable triple-peaked structure is also seen in He I λ5876 emission lines (right panel of Fig. 11). An almost identical feature is also present near 4100 Å. This could be identified as Hδ, although this is inconsistent with the weakness of Hγ and Hβ. A more likely possibility is the N III Bowen line at 4100 Å (see Sect. 3.5). These profiles may also be present in the earlier X-shooter epochs, albeit very weak. The wings of these profiles extend from $-10\,000\,\mathrm{km\,s^{-1}}$ to $12\,000\,\mathrm{km\,s^{-1}}$, so are significantly narrower than Hα and He II. This could imply that they originate in lower velocity regions of the disk, that is, farther out than Hα and He II. Their central peak also appears near rest velocity. We note that He II shows broader peaks compared to the profiles of the lower-ionisation lines. At the same time, the He II blue peak appears brighter than the red peak, which is opposite to the Hα profile. This is likely due to contamination of the Bowen N III line at 4640 Å, as quantified below.

3.5. De-blending the He II complex

As noted above, the line profiles of He II differ somewhat from those of Hα: in particular, the blue peak is either equal to or brighter than the red peak, whereas in Hα the red peak is always stronger than the blue peak.

The region around He II contains a number of emission lines that are observed in TDEs, including N III λ4640, Hβ and Fe II lines. To investigate this in more detail, we tried to fit the entire emission feature with a superposition of Gaussians for the aforementioned elements. We are not able to find consistencies in the derived parameters for the respective lines (e.g. line identification, velocity, or FWHM) if we include single Gaussian components in addition to He II.

Instead, we turn to the emission lines observed during the epoch at +10 days. In particular, the double-peaked feature centred on 4100 Å is unlikely to be Hδ, given the absence of both Hβ and Hγ. Instead, this line can be identified as a N III Bowen line. From a spectroscopic study of a sample of TDEs, it was found that the N III 4100 and 4640 Å lines have a roughly 1:1 flux ratio (Charalampopoulos et al. 2022) when they are present. Given that the 4100 Å line is readily identified in the X-shooter spectrum at +10 days, we attempt to subtract this line profile from the He II line, assuming a 1:1 flux ratio and identical velocity structure (so we assume that N III 4640 is identical to N III 4100). The red wing of the N III 4100 appears to be contaminated by another potential emission line. This feature is centred around 4250 Å, and it is not immediately clear to which element this line can be attributed. In order to not overfit the spectra, we normalised the entire UVB spectrum (in the range 3700–5250 Å) using a low order spline function, and this feature therefore remains in the normalised spectrum. The N III 4100 and He II features are shown in the top panel of Fig. 13. The contamination of N III manifests as the increasing flux trend at velocities above $10\,000\,\mathrm{km\,s^{-1}}$, and may lead to some systematic uncertainties in the fitting described later. To avoid biasing the results in the blue wing, we linearly interpolate over the Ca H+K region (shown by the dashed line in the top panel). The bottom panel of Fig. 13 shows the result of the subtraction (in blue) overlaid on the (unmodified) Hα line profile. The result of the red wing contamination leads to a somewhat narrower red wing profile in velocity space. Notwithstanding the simplifying assumptions for the various line profiles, the subtracted He II profile is remarkably similar to the Hα line profile. We conclude that AT2020zso belongs to the spectroscopic class of He+Bowen
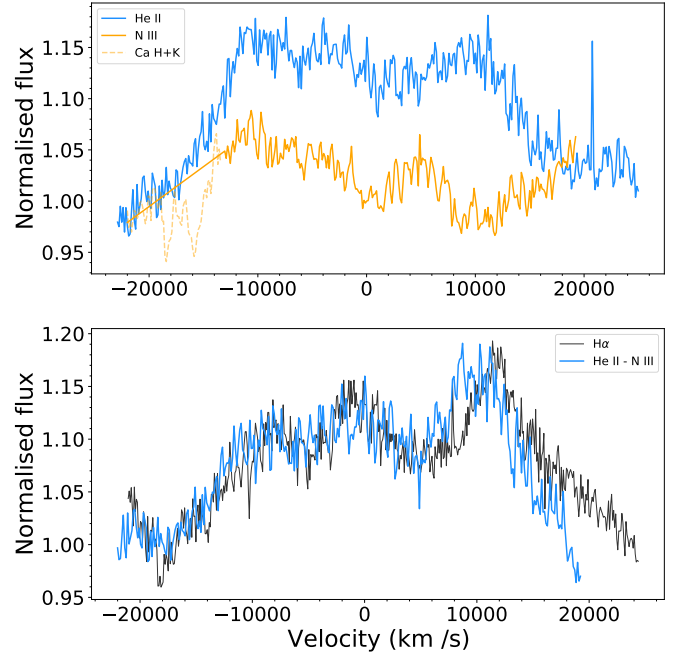

Fig. 13. Comparison of the emission line profiles. *Top panel*: He II (blue) and N III 4100 Å lines from the X-shooter spectrum at +10 days. *Bottom panel*: subtracted spectrum (He II – N III, blue) and Hα for comparison (in black). The line profiles are nearly identical, suggesting the presence of double-peaked Bowen N III lines, the first such line profiles seen in a TDE to date. The discrepancy in the red wing (compared to Hα) is likely related to the imperfect normalisation and subtraction of the N III profile.

line TDEs, and that the He II line likely originates from the same physical region as the Hα and Bowen N III lines.

We also performed the same subtraction procedure for for the X-shooter spectrum at phase –3 days and present the results in Fig. A.3 of the appendix. We use these subtracted He II line profiles for the accretion disk modelling. It is likely that the subtraction procedures introduce some systematic errors (e.g. the contamination in the red wing of N III), so we treat the fits to the Hα lines as our primary results. We also present the He II fitting results, but keeping in mind the caveats mentioned here.

3.6. Elliptical accretion disk fitting

Before we describe our model fitting results, we remind the reader that a general prediction of relativistic circular accretion disk models is that the blue peak is equal to, or brighter than, the red peak, due to Doppler boosting of emission from the region moving in our direction (e.g. Chen et al. 1989; Chen & Halpern 1989). This is no longer true for eccentric accretion disks: for non-negligible eccentricities, there exist orientation and inclination angle combinations such that the red peak can appear brighter than the blue peak. In other words, when interpreting a line profile as originating from an accretion disk, a double-peaked line profile with a dominant red peak is a strong indication of a non-axisymmetric (eccentric) configuration. There exist other mechanisms that can produce similar asymmetric line profiles, which will be discussed in Sect. 4.

Double-peaked emission lines have been observed in other TDEs, where they were interpreted as signatures of a spiral wave or an accretion disk. For the TDE with the most

convincing double-peaked emission profiles so far (AT2018hyz; Short et al. 2020; Hung et al. 2020), an almost circular geometry was derived through model fitting. In our analysis we take a similar approach to Hung et al. (2020), and attempt to fit a general relativistic accretion disk model of Eracleous et al. (1995) to the Hα and He II lines. We do not model the N III and He I lines because of their limited S/N, and furthermore we do not present modelling results for the lines in low-resolution spectra because this leads to degeneracies and inconsistent results.

This model has seven free parameters, including the emissivity power-law index q, the broadening parameter σ, the major axis orientation of the elliptical rings ϕ_0 (for 0 degrees, the nodal line is along our line of sight, and the apocentre is in our direction), the inclination angle i (where 0 degrees is face-on), the eccentricity e, and the inner and outer pericentre distances (that is the line emitting region of the disk is bounded by elliptical annuli of radii r_1 and r_2), and is described by the following specific intensity profile I_ν:

$$I_\nu = \frac{1}{4\pi} \frac{\epsilon_0\,\xi^{-q}}{\sqrt{2\pi}\sigma} \exp\left[-\frac{(\nu^2 - \nu_0^2)}{2\sigma^2}\right]. \tag{2}$$

The line profile flux $F \equiv \int d\nu \int \int d\Omega I_\nu$, that is, the integral of I_ν over frequency, specific intensity and solid angle, is calculated by numerical integration and rescaled to fit the observations. The fit is performed by varying two normalisation constants A and B, $A + B \times F$ (where $A \approx 1$ is the adjacent continuum level for each spectrum and B is the amplitude of the profile) to the data to account for small (a few per cent) differences in the normalisation level.

We focus our analysis on the X-shooter spectra as they have superior spectral resolution and S/N. The first epoch (at −13 days) is omitted, because at these early times the line emitting regions likely originate in an outflowing photosphere rather than in an accretion disk like structure (as is implied by the EW evolution and will be discussed later). We nevertheless attempted a fit for this epoch, but the results are highly degenerate and do not allow robust parameter inference. We fit each emission line profile (He II and Hα) separately, for each epoch, for a total of four fits. We use a nested MCMC sampling approach implemented in `dynesty`, with uniform priors for all parameters as summarised in Table 4. Because the computational time of this approach is proportional to the size of the parameter space, we first create a grid of ~231 000 models and perform a least-squares minimisation to assess the best-fit models. These results are used to inform the prior ranges, which are nevertheless taken very conservatively to encompass most of the plausible parameter space. Following the results presented in Hung et al. (2020), we report on the results of a composite accretion disk + outflowing component model fit to the data, where the outflow is represented by a Gaussian component.

The best-fit model parameters are presented in Table 5, and they are overlaid on the data in Fig. 14. The posterior distributions of the parameters for each fit can be found in Appendix A.

For each individual epoch, we infer global accretion disk model parameters that are very similar for the Hα and the He II profiles. This may appear somewhat surprising, given that the He II profile is significantly contaminated by N III. This indicates that the subtraction (and the 1:1 flux ratio assumption for the N III lines) performs well.

We find that the disk must be highly inclined with respect to our line of sight, that is, we are seeing it nearly edge-on ($i = 85 \pm 5$ degrees for Hα, and $i = 88 \pm 2$ for He II). The inferred eccentricity is high and consistent between Hα and

Table 4. Priors used for MCMC accretion disk plus Gaussian model fitting.

Parameter	Prior range
Emissivity index (q)	2–3
Line broadening (σ)	500–4500 km s^{-1}
Inclination (i)	0–90 degrees
Eccentricity (e)	0–1
Orientation angle (ϕ_0)	0–360 degrees
Inner radius (r_1)	100–550 R_g
Outer radius (r_2)	750–4750 R_g
A	0.95–1.05
B	0–0.2
Amplitude	0–0.125
FWHM (narrow)	0–3000 km s^{-1}
Velocity shift (narrow)	−3000–1000 km s^{-1}
FWHM (broad)	22 500–40 000 km s^{-1}
Velocity shift (broad)	−4000–4000 km s^{-1}

Notes. Values below the horizontal line pertain to the Gaussian component. An exploratory study using a grid of models covering a wide parameter range was used to determine the range of some priors.

He II, $e = 0.97 \pm 0.01$. This is very similar to the characteristic eccentricity of ballistic orbits travelled by the tidal debris, ~0.98 $[\frac{(M_{BH}/M_\star)}{10^6}]^{1/3}$, expected for returning debris whose orbit has not been significantly altered by hydrodynamics. We furthermore find largely consistent orientation angles (ϕ between 210 and 260 degrees) and line broadening parameters ($\sigma \sim 1000$–1500 km s^{-1}) for all epochs/lines. There is some scatter in the inner and outer disk radii, but this may not be surprising given the limited S/N of the data. The inner disk radius is several 100 gravitational radii, while for the outer radius we find values between 1400–2200 R_g, with one outlier at 4100 R_g. Finally, we note that while we have added a Gaussian component to the line profile fitting, in most cases the amplitude and contribution of this component is small. Only in the last epoch is there a clear triple-peaked structure. This additional component is found to be consistent with being at rest velocity, with a FWHM of 1000–2500 km s^{-1}.

In summary, we find that a highly inclined, highly elliptical accretion disk model can reproduce the Hα and He II line profiles of both epochs, with general disk parameters that are largely consistent within their uncertainties. Given the contamination He II, the fitting results are reasonably similar to those inferred from Hα.

4. Discussion

4.1. Alternative origins of the broad double-peaked emission lines

As previously indicated, there exist multiple mechanisms or structures that can explain the presence of double-peaked broad emission lines. We now discuss each of these in more detail, and why we prefer the accretion disk model as an explanation.

4.1.1. Supermassive black hole binary

An SMBH binary would spend most of its time in the hard binary phase, where the separation is typically 0.1−1 pc (10^{17-18} cm, Eracleous et al. 1995). In this scenario, the tidal field of the secondary would drive a disk around the primary to become

Table 5. Results of the MCMC accretion disk plus Gaussian model fitting.

Line	q	σ (km s^{-1})	i (°)	e	ϕ_0 (°)	r_1 (R_g)	r_2 (R_g)	Vel. (km s^{-1})	$FWHM$ (km s^{-1})	Ampl.
Hα, −13d	–	–	–	–	–	–	–	800 ± 400	37 500 ± 6500	0.02 ± 0.01
He II, −13d	–	–	–	–	–	–	–	−170 ± 135	31 000 ± 850	0.13 ± 0.01
Hα, −3d	2.41 ± 0.04	1018 ± 273	85 ± 6	0.96 ± 0.02	256 ± 2	302 ± 13	4095 ± 315	−944 ± 1019	1014 ± 957	0.02 ± 0.01
He II, −3d	2.12 ± 0.05	1570 ± 205	89 ± 1	0.97 ± 0.01	219 ± 2	121 ± 12	2250 ± 375	675 ± 380	1750 ± 650	0.02 ± 0.01
Hα, +10d	2.28 ± 0.04	1270 ± 145	78 ± 5	0.96 ± 0.02	242 ± 2	270 ± 11	1453 ± 74	−494 ± 935	2169 ± 818	0.02 ± 0.01
He II, +10d	2.92 ± 0.06	1330 ± 100	86 ± 3	0.97 ± 0.01	208 ± 1	530 ± 10	2100 ± 90	400 ± 90	2400 ± 110	0.07 ± 0.01

Notes. For completeness we also provide the results of the Gaussian-only model for the first epoch, where the accretion disk model does not provide a good fit.
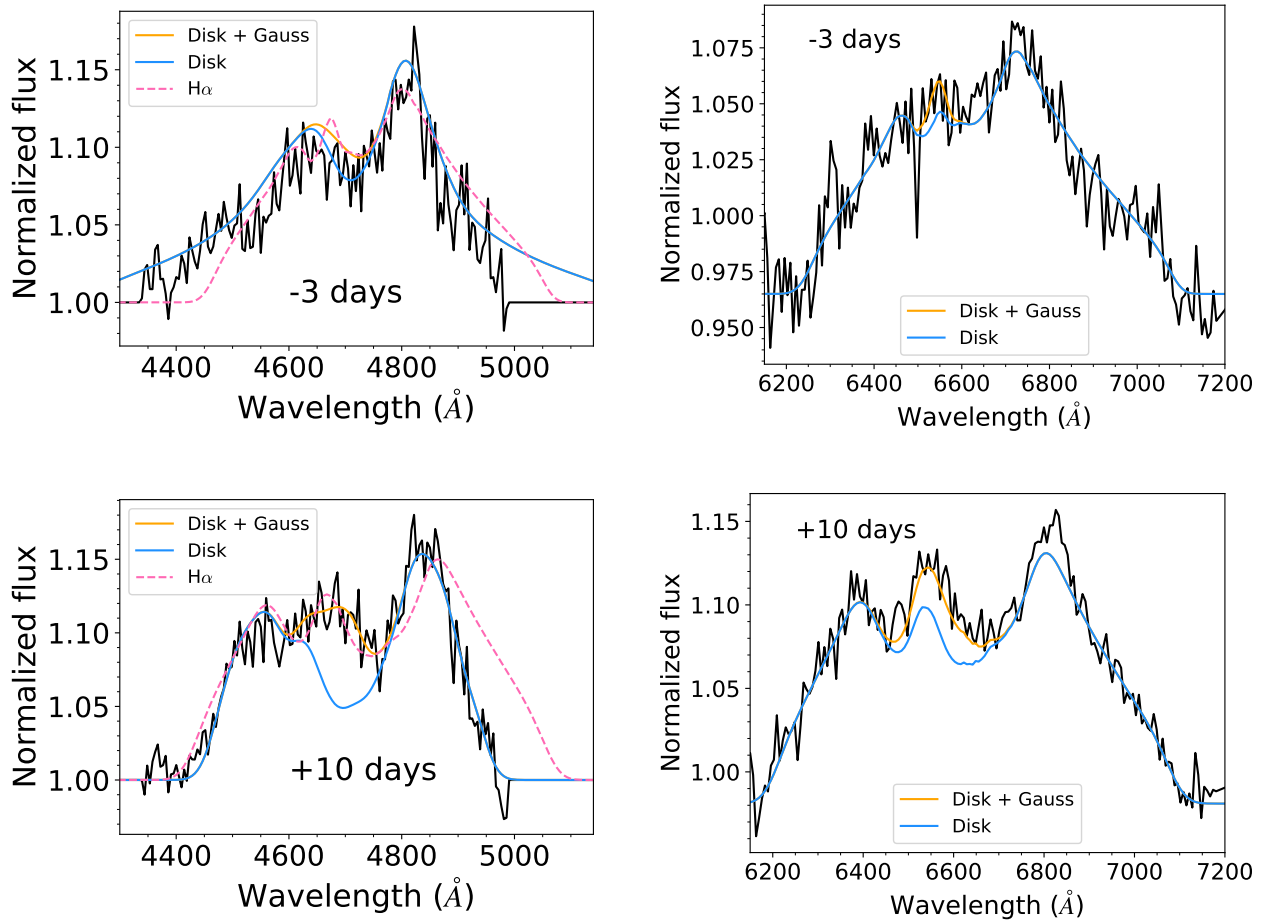

Fig. 14. Best-fit accretion disk plus Gaussian models, overlaid on the emission line profiles of He II (*left panels*) and Hα (*right panels*). Black represents the data, blue the accretion disk model, and orange the accretion disk plus outflow model. The best-fit Hα models are overplotted in the He II profiles as dashed lines for comparison. The red wing of He II is poorly subtracted, leading to some differences with the Hα profiles, but overall the results are consistent. The model parameters can be found in Table 5.

eccentric if the mass ratio is >4 (Eracleous et al. 1995). However, the timescale for this eccentricity to evolve is thousands of years, clearly inconsistent with the observed line profile variations on timescales of weeks.

We conclude that an SMBH binary alone cannot provide an explanation for the observed properties of AT 2020zso, in particular the rapid evolution of the line profiles.

4.1.2. Turn-on or changing-look AGN

One scenario that could help explain the observed properties is that rather than a newly formed accretion disk, we are see-

ing either a turn-on AGN (without the need for a tidal disruption) or a dormant, eccentric accretion disk being reinvigorated with fresh material, so an AGN turning on where a fossil accretion disk is being resupplied by the debris of a star. In either case, the binary SMBH hypothesis is then required to explain the observed eccentricity. This scenario could be consistent with the hypothesis that the primary black hole was a dormant AGN that shut off in the recent past, as inferred from the narrow line region diagnostics. In other words, the AGNs must have shut off within a light travel time (typically a few hundred years) to the narrow line region. Such timing would be coincidental; the high inferred eccentricities also imply that the origin of the

emission lines is very unlikely to be a pre-existing broad line region that is reactivated by the flare, as the values inferred from double-peaked AGN sources are typically much more modest (e.g. Eracleous et al. 1995; Strateva et al. 2003).

4.1.3. Outflows and spiral arms

Bipolar outflows can also result in double-peaked line profiles, but the brighter red-than-blue peaked profile cannot be reproduced through Doppler boosting of emission. Nevertheless, profiles similar to AT2020zso (in that they have a brighter red than blue wing) have been observed in some supernovae (Smith et al. 2015; Bose et al. 2019), although they are generally seen in Hα, not He II. It is unclear what would power the Bowen fluorescence lines in this scenario. This scenario would require an ad hoc adjustment of the relative brightness of the blue and red peaks to produce the observed variability. Furthermore, it would require the UV/optical blackbody photosphere to expand and recede independently of the outflow (as we see the former moving inwards after peak, which is incompatible with an outflow scenario powering the lines at those times). The quasi-Gaussian line profile, combined with the light curve evolution at early times suggests that any outflow present in AT 2020zso would likely have a near spherical geometry. While a wide-angle bipolar outflow can therefore not be excluded based on current data, an aspherical structure could be detectable in polarimetric observations.

Spiral structures have also been invoked to help explain the variability in double-peaked AGN sources (e.g. Storchi-Bergmann et al. 2003). This variability is typically associated with the rotation of the gas (or precession of the spiral structure) on timescales larger than several dynamical timescales. This dynamical timescale is roughly

$$t_{\rm dyn} = 2M_6\xi^{3/2} \text{ days}, \tag{3}$$

where M_6 is the black hole mass in units of $10^6 \, M_\odot$ and ξ is the disk outer radius in units of 1000 $R_{\rm g}$. This yields a value of ∼5–15 days for AT 2020zso. While this appears compatible with the observed timescales for variability, it remains unclear how such a spiral structure would form in the very brief period of time between disruption and peak light. Furthermore, this scenario generally invokes an axisymmetric disk configuration, and hence circularisation would have to be extremely rapid – not accounting for the formation timescale of the spiral structure itself. We therefore deem it unlikely that spiral arm patterns can provide a plausible explanation of the observed behaviour.

4.2. Light curve and blackbody evolution

The light curve and radius evolution are remarkably similar to other TDEs with pre-peak observations, including AT 2019qiz (Nicholl et al. 2020) and AT2019ahk (Holoien et al. 2019b): consistent with $L \propto t^2$ and constant outflow velocities of a few thousand km s^{-1}. A quasi-spherical outflow with constant velocity and temperature will lead to the observed $L \propto t^2$ behaviour. The fact that the early evolution (before the first *Swift* observations) is consistent with $L \propto t^2$ suggests that the temperature was roughly constant during this phase.

The temperature cools significantly over the first 40 days, behaviour that is similar to AT 2018hyz and ASASSN–14ae (Gomez et al. 2020) as well as ASASSN–15lh (Leloudas et al. 2016). This may be related to a comparatively low amount of debris due to a partial tidal disruption, leading to shorter diffu-

sion times (Short et al. 2020; Gomez et al. 2020) and therefore faster temperature evolution. This cooling phase may also help explain the transition from initially broad Gaussian line profiles dominated by He II to the appearance of Hα slightly later, and finally to the emergence of the double-peaked disk profiles.

The peak bolometric UV/optical luminosity reaches 7×10^{43} erg s^{-1} – this corresponds to roughly the Eddington limit of a ∼5 × 10^5 $M_\odot$ black hole, or an Eddington ratio of 0.4 for a ∼10^6 $M_\odot$ black hole. The blackbody radius (Fig. 8) reaches a maximum around 10^{15} cm, then rapidly decreases after peak light, and asymptotes to 5×10^{13} cm at late times. Assuming a 10^6 (5×10^5) $M_\odot$ black hole, the peak and late-time values correspond to approximately 3000 (6000) and 200 (400) gravitational radii, respectively. This latter value is similar to that inferred for the inner edge of the accretion disk at +10 days, indicating that the UV/optical emission at these epochs (+150 days) is consistent with being produced directly by the accretion disk. Here it is assumed that the inner disk radius does not significantly increase in size between the +10 days and +160 days epochs. We justify this assumption by noting that the accretion disk emission is dominated by the hottest, inner regions of the disk, and there are no obvious accretion related processes that would lead to an approximately order of magnitude increase in the inner disk radius. Similar behaviour has been observed in other TDEs, where the late-time UV emission (in this case meaning several years after peak light) is also found to be consistent with an accretion disk origin (van Velzen et al. 2019). In AT 2020zso, however, the accretion disk emission appears to dominate the UV bands already much earlier, similar to the TDE AT 2018fyk (Wevers et al. 2021), where rapid disk formation was inferred from other spectroscopic emission features (Wevers et al. 2019a).

Emission lines originating in an accretion disk may be collisionally excited rather than through photo-ionisation. This can have a profound effect on the Balmer decrement (Hα/Hβ line ratio), as this depends sensitively on the temperature (see e.g. Fig. 11 in Short et al. 2020). If the temperature in AT2020zso was lower than in AT2018hyz, this may help to explain the weakness or absence of both Hβ and Hγ lines. As noted in Short et al. (2020), the typical blackbody temperatures in TDEs (and also in AT2020zso) are much higher than those inferred from the Balmer decrement, so the accretion disk must be significantly cooler than the blackbody emission. An alternative explanation may be that the blackbody modelling, while empirically a good fit to the data, is not intrinsically related to the observed SED shape. In this case, the inferred blackbody temperatures do not represent physical temperatures of the emitting regions.

Finally, we highlight the peculiar early time light curve evolution, with evidence for a clear break at very early times in the ZTF *g*- and *r*-band light curves from a $L \propto t^2$ behaviour to a slower evolution afterwards. Unfortunately, we do not have temperature information at the earliest times before the change in behaviour. If the outflow did not cool significantly initially, a homologously expanding outflow would be consistent with the $L \propto t^2$ evolution. This could imply the presence of an additional source of energy injection to keep the material from cooling at the earliest times. We speculate that this may be provided by the initial debris self-intersection and/or disk formation processes. Once the bulk of this energy is radiated, the further evolution is dominated by cooling as the envelope expands. Verifying such a scenario will necessitate observational constraints on the temperature evolution shortly after disruption in future TDEs. Alternatively, non-spherical expansion may also result in

differences from the canonical $L \propto t^2$ evolution before the peak in TDEs.

4.3. Evolution in the context of the accretion disk model

The blackbody emission likely has two components: a reprocessing envelope and an accretion disk.

At phase -14 days, the expanding outflow is very likely reprocessing the X-rays produced at very small scales (whose presence is inferred from the presence of Bowen lines). This outflow provides the dominant contribution to the emission lines before peak, gradually decreasing as the material becomes optically thin. The spectrum is hence dominated by very broad Gaussian-like signatures, the hall-mark sign of TDEs. The accretion disk at this time is weak, either contained within the expanding photosphere or still assembling. For this reason, there are not yet any double-peaked signatures in the spectra.

This evolution is consistent with the evolution of the EW ratio of He II/Hα. Shortly after our observations begin, the Hα line emerges, that is, the EW ratio decreases rapidly. This apparent evolution from H-poor to H-rich is a natural consequence of an expanding reprocessing envelope (Roth & Kasen 2018), where Hα suffers from more self-absorption when the envelope is more compact (while He II photons can escape unimpeded). As the envelope expands and cools, Hα becomes less self-absorbed and its EW increases, while the He II emitting region, located closer to the central ionising source, does not change significantly. This process has been observed in several TDEs to explain the evolution of H-rich to H-poor as the outflowing photosphere contracts after peak light (Nicholl et al. 2019; Charalampopoulos et al. 2022), but here we show that this process is very likely also at work at very early times when the envelope first starts expanding.

Around peak light, when the envelope has expanded sufficiently such that it becomes optically thin, the reprocessing becomes much more inefficient. The blackbody (continuum) emission is now a superposition of both the reprocessing outflowing layer (weakening contribution) and the accretion disk (increasing contribution). The envelope is no longer optically thick, so the spectra are dominated by the accretion disk; they show broad double-peaked emission lines that are now visible due to the large contrast with the host galaxy at peak brightness. If the outflowing photosphere was still partially optically thick at -3 days, it may contribute to the spectrum as a low amplitude, broad Gaussian. We speculate that this could help explain the peculiar outer disk radius evolution. As shown in Fig. 8, this outer radius is very similar to the blackbody radius at that epoch. Given the limited S/N of the spectrum, the contribution of the outflow may be below the level that can be detected during the fitting. When the outflow reaches its maximum extent and becomes completely optically thin at $\approx +5$ days, there is no more contamination in the last X-shooter spectrum at $+10$ days, and the outer radius as inferred from the modelling reflects the true accretion disk outer edge.

Because the mass fall-back rate scales as a negative power-law with time (and this is what mainly powers the accretion disk emission), after peak the contrast with the host starts to decrease. The continuum emission of the accretion disk remains visible in the UV (even at phases $+150$ days; see Fig. 1) because of the higher contrast with the host (see the host SED in Fig. 2), whereas the optical (continuum as well as line) emission falls below the host level. As a result, the black-body UV (continuum) emission remains visible, but the optical spectra no longer shows emission line signatures of the disk.

4.4. A rapidly formed, elliptical accretion disk

The Hα and He II emission line profiles display a prominent asymmetry, contrary to predictions from relativistic, circular accretion disks. Warped disks are also able to produce brighter red-than-blue profiles if the warp preferentially obscures the blue-shifted side of the disk. Our fitting results show that the line profiles can be well reproduced by eccentric, inclined relativistic disk models. We fitted all epochs and lines independently and find consistent values for the main disk parameters despite the significant line profile variability that is observed on approximately two-week timescales. We focus below on the results from Hα modelling, given the potential systematic uncertainties introduced by de-blending the He II region.

The line broadening parameter σ is not expected to strongly influence the line profiles (Eracleous et al. 1995); we find values $\sim 1000-2000$ km s^{-1} for both Hα and He II. Similarly, the inferred inclinations and orientation angles agree well for all epochs and lines (average $i = 85$ degrees and average $\phi_0 = 240$ degrees). The inner and outer radii are largely consistent with theoretical expectations for TDE disks, predicted to be more compact in nature than, for example, AGN disks. Figure 8 shows that the peak of the inferred (expanding) blackbody radius coincides roughly with the outer extent of the disk at a similar epoch. Similarly, at late times the blackbody radius is of the same order as the disk inner and outer radii. This comparison is somewhat ambiguous, as we compare the radii of an elliptical structure (the accretion disk) with a spherical structure (implicitly assumed when calculating the blackbody radius). We stress that this is an order of magnitude comparison only.

It has been shown, on theoretical grounds, that the initial debris following the tidal disruption of a star is distributed on highly eccentric rings, and that this eccentricity may be long-lived (e.g. Syer & Clarke 1992, 1993; Zanazzi & Ogilvie 2020). Hydrodynamical models have further corroborated the picture where an eccentric, extended disk forms around the time when the mass return rate peaks (Shiokawa et al. 2015; Piran et al. 2015; Krolik et al. 2016). A complicating factor in the identification of such a structure is the presence of an optically thick wide-angle outflow at early times (e.g. Sądowski et al. 2016). While it is theoretically unclear if, and if so how quickly, the debris can shed its orbital energy and form a disk (Guillochon et al. 2014; Bonnerot & Lu 2020), observationally it is now well-established that an accretion disk can form on $\sim$month timescales (Short et al. 2020; Hung et al. 2020; Cannizzaro et al. 2021; Wevers et al. 2019a, 2021) in line with hydrodynamical simulations. In the case of AT 2018hyz, accretion disk modelling similar to that performed here was used to infer a quasi-circular structure ($e \approx 0.1$) around 50 days after the peak of the light curve (Hung et al. 2020). Here, we establish the presence of an elliptical accretion disk around peak light, around one month after disruption, providing further evidence that in spite of the theoretical uncertainties and our lack of understanding of the post-disruption dynamics, an accretion disk can form very quickly.

The compact, elliptical nature of the accretion disk in AT2020zso is in contrast with the majority of the literature, in which it is often assumed that apsidal precession (or some other mechanism) will quickly remove orbital energy from the debris, leading to a nearly circular orbit on the scale of the tidal

radius. Instead, our findings suggest a highly eccentric structure with a semi-major axis of ~100 times the tidal radius, similar to that found by hydrodynamical simulations (e.g. Shiokawa et al. 2015).

AT 2020zso is the first TDE where it can be quantitatively confirmed that the initial debris maintains highly eccentric orbits for a significant amount of time. Due to the lack of observational data before the peak in other TDEs, it remains unclear how often this occurs, that is, if inefficient circularisation is common among TDEs. Krolik et al. (2020) argue that whether or not circularisation is efficient depends sensitively on the pericentre radius of the fatal orbit, with circular accretion disks being a rare occurrence.

Future observations of double-peaked emission lines covering pre- and post-peak phases, where disk signatures can be identified unambiguously throughout the evolution, are necessary to establish the eccentricity evolution of TDE disks in more detail.

4.5. Bowen lines and the TDE unification model

We have confirmed AT2020zso as a TDE with Bowen emission features – and the first with double-peaked Bowen lines. The excitation of these lines requires a strong soft X-ray or extreme ultra-violet (EUV) source, as they are powered through a recombination cascade including He II. However, Leloudas et al. (2019) found that the majority of Bowen-strong TDEs were not detected at X-ray wavelengths. In the TDE unification model of Dai et al. (2018), the properties of Bowen-strong TDEs can be explained if the inclination of the newly formed accretion disk is closer to edge-on than face-on. For Eddington ratios of $L_{Edd} > 0.1$, the accretion disk is likely slim rather than thin, leading to an optically thick barrier (potentially aided by an optically thick outflow) that results in strong suppression of X-ray photons for an outside observer.

The presence of double-peaked Bowen lines implies that they are formed very close to the accretion disk surface, most likely in the same region as the He II and Hα emitting regions. With a peak UV/optical Eddington ratio of ≈0.5 for AT2020zso, the disk likely has a slim geometry. Combined with the very high inclination angle (~85 degrees) this may provide the dense gas that produces the Bowen lines through X-ray irradiation, while at the same time explaining the lack of observed X-ray emission by *Swift*. This provides the first direct confirmation (albeit for a single source) that the orientation of Bowen-strong TDEs is indeed near edge-on, and the unification model laid out by Dai et al. (2018) and Leloudas et al. (2019) is consistent with these results. The high inclination of the newly formed disk may also help explain the lack of intrinsic (as well as TDE) X-ray emission at early and late times – we derived a lower limit for the column density of 10^{22} cm^{-2} to reconcile the observed X-ray upper limit with the expected AGN X-ray luminosity at late times. Such a column could be provided by a high inclination compact accretion disk.

4.6. Comparison to double-peaked TDEs and AGNs

The elliptical accretion disk model that we have employed has been extensively used in the literature for fitting AGN optical emission lines. Typically, it is applied to the (low-ionisation) double-peaked Balmer emission lines, from which parameters are extracted and analysed. We can therefore compare our own results, obtained from fitting Hα in particular, to the typical values inferred for AGN accretion disks. Figure 15 com-
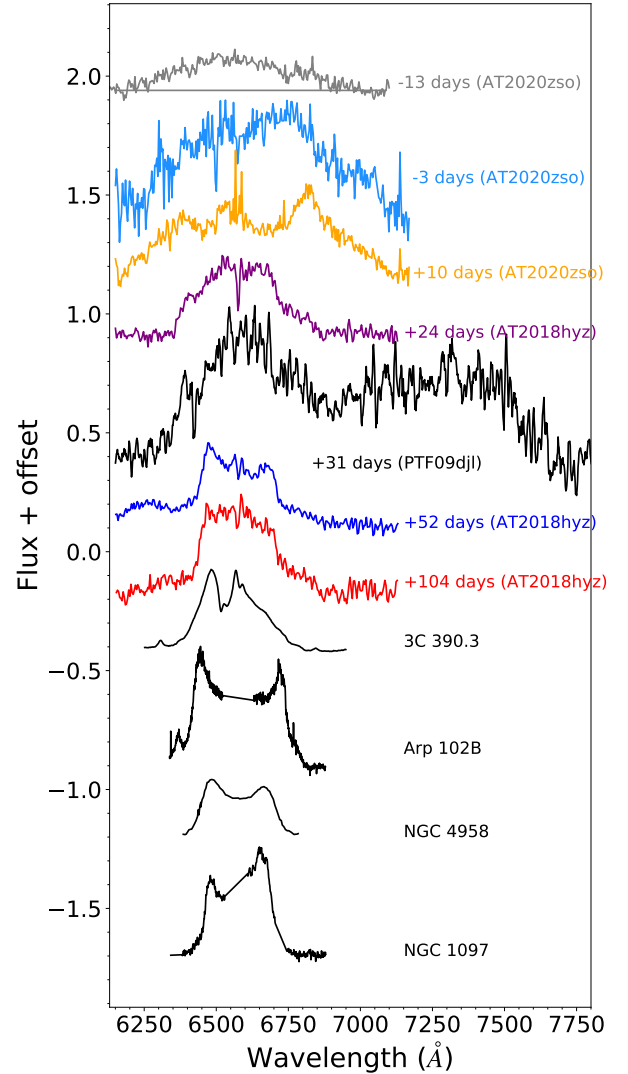

Fig. 15. Comparison between the known double-peaked TDE spectra at various epochs and double-peaked AGN sources. The grey horizontal line denotes the continuum level for clarity in the top spectrum. Data for NGC 1097 are from Schimoia et al. (2015), for NGC 4958 from Ricci & Steiner (2019), for Arp 102B from Couto et al. (2013), for AT2018hyz from Short et al. (2020), and for PTF–09djl are from Arcavi et al. (2014).

pares double-peaked TDE spectra at different phases with some double-peaked AGN spectra. Considering only the TDE spectra, it becomes apparent that different disk parameters have very different observational signatures. In particular the inclination of the system with respect to the line of sight can dramatically alter the line widths (AT 2018hyz has an inferred inclination angle of ~50−60 degrees, whereas both AT 2020zso and PTF–09djl have inclinations >80 degrees).

While the emissivity profile indices (between 2–3), line broadening parameters (1000–2000 km s^{-1}) and the outer radii (1500–10 000R_g) we find are typical of AGN samples (Eracleous et al. 1995; Strateva et al. 2003; Storchi-Bergmann et al. 2017), the inner radii we find are significantly smaller (typically $> 500 R_g$ for AGNs). This is in line with theoretical expectations, which predict that the stellar debris will form an accretion disk with a size of about twice the fatal orbit pericentre (of the order of several tens of gravitational

radii). It is also consistent with the much broader emission lines observed in AT 2020zso.

One notable feature of the transient emission is the presence of double-peaked high-ionisation lines, He II and N III $\lambda4640$. To our knowledge, these are the first high-ionisation line with an observed geometry similar to Hα in both TDEs and AGNs. In AGNs, double-peaked profiles are observed in low-ionisation lines such as the Balmer lines and sometimes Mg II, but no clear double-peaked profiles have been found yet in the (high-ionisation) UV resonance lines (Eracleous et al. 2009). This may be related to the (typically) much higher optical depth in the high-ionisation lines, which are thought to form in the densest parts of the accretion disk (wind). The likeness of He II to Hα suggests that the optical depth in both lines is similar, and hence they originate from largely the same physical region, as we infer from our accretion disk modelling.

Finally, we find marginal evidence for an additional Gaussian component near systemic velocity, with a width of $\sim1000-2000$ km s^{-1}, for the epoch at +10 days (Fig. 14). This component is very similar to the geometries found for Seyfert 1 galaxies with double-peaked emission lines (Ho et al. 1997; Schimoia et al. 2017; Storchi-Bergmann et al. 2017); it can be interpreted as originating in clouds outside of the accretion disk or outside of the disk plane (e.g. produced from a slow accretion disk wind), and hence they have lower velocity widths and are found near rest velocity. This component appears variable, as it does not appear prominently in the spectra around peak light whereas the triple peaked structure is very clear at +16 days. The difference of this component between the Hα and He II spectra is likely a result of a degeneracy with the additional Gaussian model, leading to a slightly different inferred orientation angle (this component prominently appears for $\phi > 230$ degrees). In the interpretation as a disk wind, this variability could be intrinsic: if the wind is initially optically thin (and hence appears as a weak contribution to the overall flux) but over time intensifies (e.g. if the disk reaches a steady state) and becomes optically thick, it will become stronger over time. Alternatively, the wind component may remain steady, but because it is superposed onto the accretion disk contribution (which is observed to diminish over time) it appears variable, becoming more prominent as the accretion disk flux decreases. Our spectra are not of sufficient quality (in terms of S/N) to distinguish between these scenarios.

Higher S/N, medium-resolution spectroscopy ($R \gtrsim 5000$) of future double-peaked TDEs can help shed more light on the presence and evolution of this component.

4.7. Constraints on the precession and alignment timescales and black hole spin

On the one hand, the late-time optical spectrum taken with X-shooter (215 days after peak) shows that there is no evidence for persistent broad emission lines, neither in the optical nor in the NIR. On the other hand, the blackbody radii that we derive for the UV/optical emission component is 10^{14-15} cm (Fig. 7), well inside typical torus size scales ($\gtrsim10^{16-18}$ cm, Suganuma et al. 2006; Hickox & Alexander 2018). This suggest that any obscuration must be comparatively low, certainly lower than values observed in Seyfert 2 AGNs (typically in excess of $A_V > 5$ mag; e.g. Burtscher et al. 2016; Schnorr-Müller et al. 2016). Hence, a type 2 (heavily obscured) AGN configuration is hard to reconcile with the observed photometric and spectral evolution. The implication is that any pre-existing structure, assuming it is aligned perpendicular to the black hole spin vector, has at most a moderate inclination ($<40-60$ degrees) with respect to our line of sight.

From our modelling results, we have inferred a very high (~80 degrees) inclination for the newly formed TDE disk. If it is indeed the case that the torus and any pre-existing accretion disk structures are located in a plane perpendicular to the black hole spin vector, this implies a significant misalignment between the black hole spin axis and the new disk, even after peak light. Such misaligned configurations lead to relativistic torques and so-called Lense-Thirring precession, which will tend to align the newly formed disk with the black hole spin vector as the black hole mass is orders of magnitude larger than the disrupted star.

Our spectroscopic observations can therefore be used to constrain a minimum decay timescale for the misalignment, which depends sensitively on the black hole spin and disk viscosity, as well as weakly on the black hole mass (Franchini et al. 2016; Zanazzi & Lai 2019). Rigid body precession occurs if the local precession period is longer than the sound crossing time, and simulations suggest that this is the case for a large part of parameter space typical for TDEs (Franchini et al. 2016; Zanazzi & Lai 2019). The time between the two observing epochs (~15 days), for which we infer no significant changes in inclination, eccentricity or disk orientation angle, can therefore be interpreted as an absolute lower limit to the alignment timescale. Ignoring for the moment the (small) effect of black hole mass, with these (very) conservative estimates we can already rule out spin values in excess of $a > 0.8$ for the central black hole, regardless of disk viscosity (see e.g. Fig. 12 in Franchini et al. 2016).

Longer spectral series may in the future be used to constrain changes in disk inclination. This can, in turn, provide an alternative way to constrain the disk alignment timescales (typically constrained through the detection of X-ray variability such as quasi-periodic oscillations; e.g. Pasham et al. 2019). These alignment timescales then provide a new method (see e.g. Leloudas et al. 2016; Pasham et al. 2019; Mummery & Balbus 2020b) to constrain the black hole spin and/or disk viscosity.

5. Summary

AT 2020zso is a nuclear transient classified as a TDE based on its UV/optical photometric and spectroscopic properties and evolution. We summarise the main results reported in this study as follows:

– The host galaxy has an AGN, based on the emission line content and narrow line region diagnostics (BPT diagram). From the host galaxy velocity dispersion, as well as light curve modelling, we infer a black hole mass of $5-10 \times 10^5$ $M_\odot$.

– Near-infrared photometric observations show no evidence for a light echo ~180 days after the UV/optical peak.

– The spectra show transient, asymmetric double-peaked line profiles in He II and Hα. These lines significantly evolve from the -14 days before peak light to +14 days post-peak, for which there is spectral coverage, and similar line profiles also become apparent in the He I $\lambda5876$ and N III Bowen lines ($\lambda\lambda4100, 4640$). The He II and Bowen profiles are, to our knowledge, the first high-ionisation double-peaked lines observed in an accreting SMBH.

– Light curve modelling indicates that AT 2020zso may have been the result of a partial stellar disruption. This was also the case for AT 2018hyz, another TDE that showed prominent double-peaked Balmer emission lines. This commonality may suggest that the accretion disk was visible directly due to a low amount of obscuring material, compared to more typical full stellar disruptions.

– The low amount of debris resulting from a partial disruption can also help explain the relatively rapid observed blackbody

cooling as a consequence of shorter diffusion times in the optically thick envelope. At the same time, this can also explain the rapid spectroscopic evolution: the spectra are initially He-dominated when the envelope is hottest and densest; as it expands and cools, Hα strengthens; and finally, when the debris becomes optically thin near peak light, the double-peaked disk profiles appear.

- Modelling the emission line profiles with an elliptical accretion disk model, we find that the system is highly elliptical and highly inclined (nearly edge-on). From independent fits of He II and Hα at two epochs (−3 and +10 days with respect to peak light), we infer consistent disk parameters such as the inclination and orientation angles, emissivity profiles, line broadening parameters, and inner and outer radii. The consistency between independent fits strengthens the conclusion that the eccentricity in the accretion disk is long-lived.

- The high inferred inclination (a nearly edge-on orientation), combined with the presence of Bowen fluorescence lines and the lack of observed X-ray emission, is consistent with the unification picture of TDEs, where the inclination angle largely determines the observational appearance across wavelengths. To our knowledge, this is the first direct confirmation of this theoretical picture.

- The presence of double-peaked emission lines originating in an accretion disk before peak light confirms that an accretion disk can form very quickly and efficiently (~1 month after disruption), in contrast to theoretical predictions and simulations. This indicates that our current knowledge of the post-disruption debris is far from complete.

- Around 150 days after the peak, the size of the blackbody radius, as inferred from the light curve, is consistent with the size of the accretion disk inferred from spectroscopic modelling (assuming it is similar to the values inferred at +14 days). This suggests that the UV emission may already be dominated by the accretion disk early on in the evolution.

- We use, for the first time, the lack of change in inclination as inferred from the spectroscopic signatures to constrain the alignment timescale of the newly formed disk with the black hole spin vector. This provides a novel way to probe disk precession in TDEs through spectroscopic monitoring. We find that high black hole spin values ($a > 0.8$) can be ruled out for the inferred black hole mass.

This work provides a strong link between TDEs and the elliptical accretion disks that are often inferred to explain the asymmetric double-peaked profiles in AGNs. However, the timescales for which these emission lines are visible for both types of sources are vastly different (hundreds of days for TDEs versus decades for AGNs), likely as a result of the rapidly decreasing mass accretion rate following a TDE. Hence, it remains unclear at present if TDEs can also be held responsible for the long-lived asymmetric disk structures observed in some AGNs – a steady influx of material into the elliptical disk is required for the emission lines to remain visible for prolonged periods of time.

Future observations of TDEs with double-peaked line profiles will help shed more light on the post-debris dynamics, including the efficiency of disk formation and subsequent circularisation, as well as on the connection between TDEs and double-peaked AGN sources.

References

Alexander, K. D., Velzen, S. V., Miller-Jones, J., et al. 2021, Trans. Name Server AstroNote, 24, 1
Arcavi, I., Gal-Yam, A., Sullivan, M., et al. 2014, ApJ, 793, 38
Baldwin, J. A., Phillips, M. M., & Terlevich, R. 1981, PASP, 93, 5
Becker, A. 2015, HOTPANTS: High Order Transform of PSF ANd Template Subtraction Astrophysics Source Code Library [record ascl:1504.004]
Begelman, M. C., Blandford, R. D., & Rees, M. J. 1980, Nature, 287, 307
Bianchi, L., Herald, J., Efremova, B., et al. 2011, Ap&SS, 335, 161
Blanton, M. R., & Roweis, S. 2007, AJ, 133, 734
Blecha, L., Loeb, A., & Narayan, R. 2013, MNRAS, 429, 2594
Bonnerot, C., & Lu, W. 2020, MNRAS, 495, 1374
Bose, S., Dong, S., Elias-Rosa, N., et al. 2019, ApJ, 873, L3
Burtscher, L., Davies, R. I., Graciá-Carpio, J., et al. 2016, A&A, 586, A28
Calzetti, D., Armus, L., Bohlin, R. C., et al. 2000, ApJ, 533, 682
Cannizzaro, G., Wevers, T., Jonker, P. G., et al. 2021, MNRAS, 504, 792
Cao, R., Liu, F. K., Zhou, Z. Q., Komossa, S., & Ho, L. C. 2018, MNRAS, 480, 2929
Cappellari, M. 2017, MNRAS, 466, 798
Charalampopoulos, P., Leloudas, G., Malesani, D. B., et al. 2022, A&A, 659, A34
Chen, K., & Halpern, J. P. 1989, ApJ, 344, 115
Chen, K., Halpern, J. P., & Filippenko, A. V. 1989, ApJ, 339, 742
Conroy, C., Gunn, J. E., & White, M. 2009, ApJ, 699, 486
Couto, G. S., Storchi-Bergmann, T., Axon, D. J., et al. 2013, MNRAS, 435, 2982
Cutri, R. M., Skrutskie, M. F., van Dyk, S., et al. 2003, VizieR Online Data Catalog: II/246
Dai, L., McKinney, J. C., Roth, N., Ramirez-Ruiz, E., & Miller, M. C. 2018, ApJ, 859, L20
Eracleous, M., & Halpern, J. P. 1994, ApJS, 90, 1
Eracleous, M., & Halpern, J. P. 2003, ApJ, 599, 886
Eracleous, M., Livio, M., Halpern, J. P., & Storchi-Bergmann, T. 1995, ApJ, 438, 610
Eracleous, M., Lewis, K. T., & Flohic, H. M. L. G. 2009, New Astron. Rv., 53, 133
Foreman-Mackey, D., Hogg, D. W., Lang, D., & Goodman, J. 2013, PASP, 125, 306
Forster, F., Bauer, F. E., Munoz-Arancibia, A., et al. 2020, Transient Name Server Discovery Report 2020-3449, 1
Franchini, A., Lodato, G., & Facchini, S. 2016, MNRAS, 455, 1946
Gaia Collaboration (Brown, A. G. A., et al.) 2021, A&A, 649, A1
Gaskell, C. M. 1983, in Liege International Astrophysical Colloquia, ed. J. P. Swings, 24, 473
Gezari, S., Halpern, J. P., & Eracleous, M. 2007, ApJS, 169, 167

Goad, M., & Wanders, I. 1996, ApJ, 469, 113
Gomez, S., Nicholl, M., Short, P., et al. 2020, MNRAS, 497, 1925
Gromadzki, M., Ihanec, N., Wevers, T., et al. 2020, Trans. Name Server AstroNote, 233, 1
Guillochon, J., & Ramirez-Ruiz, E. 2013, ApJ, 767, 25
Guillochon, J., Manukian, H., & Ramirez-Ruiz, E. 2014, ApJ, 783, 23
Guillochon, J., Nicholl, M., Villar, V. A., et al. 2018, ApJS, 236, 6
Hammerstein, E., Gezari, S., van Velzen, S., et al. 2021, ApJ, 908, L20
Heckman, T. M., Ptak, A., Hornschemeier, A., & Kauffmann, G. 2005, ApJ, 634, 161
Hickox, R. C., & Alexander, D. M. 2018, ARA&A, 56, 625
Ho, L. C., Filippenko, A. V., & Sargent, W. L. W. 1997, ApJS, 112, 315
Hodgkin, S. T., Harrison, D. L., Breedt, E., et al. 2021, A&A, 652, A76
Holoien, T. W. S., Huber, M. E., Shappee, B. J., et al. 2019a, ApJ, 880, 120
Holoien, T. W. S., Vallely, P. J., Auchettl, K., et al. 2019b, ApJ, 883, 111
Hung, T., Cenko, S. B., Roth, N., et al. 2019, ApJ, 879, 119
Hung, T., Foley, R. J., Ramirez-Ruiz, E., et al. 2020, ApJ, 903, 31
Johnson, B. D., Leja, J., Conroy, C., & Speagle, J. S. 2021, ApJS, 254, 22
Kewley, L. J., Dopita, M. A., Sutherland, R. S., Heisler, C. A., & Trevena, J. 2001, ApJ, 556, 121
Kewley, L. J., Groves, B., Kauffmann, G., & Heckman, T. 2006, MNRAS, 372, 961
Kormendy, J., & Ho, L. C. 2013, ARA&A, 51, 511
Krolik, J., Piran, T., Svirski, G., & Cheng, R. M. 2016, ApJ, 827, 127
Krolik, J., Piran, T., & Ryu, T. 2020, ApJ, 904, 68
Law-Smith, J., Ramirez-Ruiz, E., Ellison, S. L., & Foley, R. J. 2017, ApJ, 850, 22
Leloudas, G., Fraser, M., Stone, N. C., et al. 2016, Nat. Astron., 1, 0002
Leloudas, G., Dai, L., Arcavi, I., et al. 2019, ApJ, 887, 218
Liu, G., Zakamska, N. L., Greene, J. E., Nesvadba, N. P. H., & Liu, X. 2013, MNRAS, 436, 2576
Liu, F. K., Zhou, Z. Q., Cao, R., Ho, L. C., & Komossa, S. 2017, MNRAS, 472, L99
Masci, F. J., Laher, R. R., Rusholme, B., et al. 2019, PASP, 131, 018003
McConnell, N. J., & Ma, C.-P. 2013, ApJ, 764, 184
McMahon, R. G., Banerji, M., Gonzalez, E., et al. 2013, The Messenger, 154, 35
Million, C., Fleming, S. W., Shiao, B., et al. 2016, ApJ, 833, 292
Mockler, B., Guillochon, J., & Ramirez-Ruiz, E. 2019, ApJ, 872, 151
Mummery, A., & Balbus, S. A. 2020a, MNRAS, 492, 5655
Mummery, A., & Balbus, S. A. 2020b, MNRAS, 497, L13
Nevin, R., Comerford, J., Müller-Sánchez, F., Barrows, R., & Cooper, M. 2016, ApJ, 832, 67
Nicholl, M., Blanchard, P. K., Berger, E., et al. 2019, MNRAS, 488, 1878
Nicholl, M., Wevers, T., Oates, S. R., et al. 2020, MNRAS, 499, 482
Norman, C., & Miley, G. 1984, A&A, 141, 85
Pasham, D. R., Remillard, R. A., Fragile, P. C., et al. 2019, Science, 363, 531
Piran, T., Svirski, G., Krolik, J., Cheng, R. M., & Shiokawa, H. 2015, ApJ, 806, 164
Planck Collaboration XVI. 2014, A&A, 571, A16
Prochaska, J. X., Hennawi, J., Cooke, R., et al. 2020a, https://doi.org/10.5281/zenodo.3743493
Prochaska, J. X., Hennawi, J. F., Westfall, K. B., et al. 2020b, J. Open Source Softw., 5, 2308
Ricci, T. V., & Steiner, J. E. 2019, MNRAS, 486, 1138
Roth, N., & Kasen, D. 2018, ApJ, 855, 54
Ryu, T., Krolik, J., & Piran, T. 2020a, ApJ, 904, 73
Ryu, T., Krolik, J., Piran, T., & Noble, S. C. 2020b, ApJ, 904, 100
Sądowski, A., Tejeda, E., Gafton, E., Rosswog, S., & Abarca, D. 2016, MNRAS, 458, 4250
Schawinski, K., Urry, C. M., Simmons, B. D., et al. 2014, MNRAS, 440, 889
Schimoia, J. S., Storchi-Bergmann, T., Grupe, D., et al. 2015, ApJ, 800, 63
Schimoia, J. S., Storchi-Bergmann, T., Winge, C., Nemmen, R. S., & Eracleous, M. 2017, MNRAS, 472, 2170
Schlafly, E. F., & Finkbeiner, D. P. 2011, ApJ, 737, 103
Schnorr-Müller, A., Davies, R. I., Korista, K. T., et al. 2016, MNRAS, 462, 3570
Shiokawa, H., Krolik, J. H., Cheng, R. M., Piran, T., & Noble, S. C. 2015, ApJ, 804, 85
Short, P., Nicholl, M., Lawrence, A., et al. 2020, MNRAS, 498, 4119
Smartt, S. J., Valenti, S., Fraser, M., et al. 2015, A&A, 579, A40
Smette, A., Sana, H., Noll, S., et al. 2015, A&A, 576, A77
Smith, J. A., Tucker, D. L., Kent, S., et al. 2002, AJ, 123, 2121
Smith, N., Mauerhan, J. C., Cenko, S. B., et al. 2015, MNRAS, 449, 1876
Smith, K. W., Smartt, S. J., Young, D. R., et al. 2020, PASP, 132, 085002
Speagle, J. S. 2020, MNRAS, 493, 3132
Storchi-Bergmann, T., Nemmen da Silva, R., Eracleous, M., et al. 2003, ApJ, 598, 956
Storchi-Bergmann, T., Schimoia, J. S., Peterson, B. M., et al. 2017, ApJ, 835, 236

Strateva, I. V., Strauss, M. A., Hao, L., et al. 2003, AJ, 126, 1720
Suganuma, M., Yoshii, Y., Kobayashi, Y., et al. 2006, ApJ, 639, 46
Svirski, G., Piran, T., & Krolik, J. 2017, MNRAS, 467, 1426
Syer, D., & Clarke, C. J. 1992, MNRAS, 255, 92
Syer, D., & Clarke, C. J. 1993, MNRAS, 260, 463
Valenti, S., Howell, D. A., Stritzinger, M. D., et al. 2016, MNRAS, 459, 3939
van Dokkum, P. G., Bloom, J., & Tewes, M. 2012, L.A.Cosmic: Laplacian Cosmic Ray Identification Astrophysics Source Code Library, [record ascl:1207.005]
van Velzen, S., Stone, N. C., Metzger, B. D., et al. 2019, ApJ, 878, 82
van Velzen, S., Gezari, S., Hammerstein, E., et al. 2021, ApJ, 908, 4
Wevers, T., van Velzen, S., Jonker, P. G., et al. 2017, MNRAS, 471, 1694
Wevers, T., Pasham, D. R., van Velzen, S., et al. 2019a, MNRAS, 488, 4816
Wevers, T., Stone, N. C., van Velzen, S., et al. 2019b, MNRAS, 487, 4136
Wevers, T., Pasham, D. R., van Velzen, S., et al. 2021, ApJ, 912, 151
Zanazzi, J. J., & Lai, D. 2019, MNRAS, 487, 4965
Zanazzi, J. J., & Ogilvie, G. I. 2020, MNRAS, 499, 5562
Zheng, W., Binette, L., & Sulentic, J. W. 1990, ApJ, 365, 115

[1] European Southern Observatory, Alonso de Córdova 3107, Casilla 19, Santiago, Chile
e-mail: twevers@eso.org
[2] Birmingham Institute for Gravitational Wave Astronomy and School of Physics and Astronomy, University of Birmingham, Birmingham B15 2TT, UK
[3] Department of Physics and Astronomy, Johns Hopkins University, 3400 N. Charles St., Baltimore, MD 21218, USA
[4] DTU Space, National Space Institute, Technical University of Denmark, Elektrovej 327, 2800 Kgs. Lyngby, Denmark
[5] Warsaw University Astronomical Observatory, Al. Ujazdowskie 4, 00-478 Warszawa, Poland
[6] Department of Physics and Astronomy, University of Turku, 20014 Turku, Finland
[7] The School of Physics and Astronomy, Tel Aviv University, Tel Aviv 69978, Israel
[8] CIFAR Azrieli Global Scholars program, CIFAR, Toronto, Canada
[9] Department of Astrophysics/IMAPP, Radboud University, PO Box 9010, 6500 GL Nijmegen, The Netherlands
[10] SRON, Netherlands Institute for Space Research, Sorbonnelaan 2, 3584 CA Utrecht, The Netherlands
[11] The Oskar Klein Centre, Department of Astronomy, Stockholm University, AlbaNova 10691, Stockholm, Sweden
[12] School of Physics & Astronomy, Cardiff University, Queens Buildings, The Parade, Cardiff CF24 3AA, UK
[13] Finnish Centre for Astronomy with ESO (FINCA), 20014 University of Turku, Finland
[14] Tuorla Observatory, Department of Physics and Astronomy, 20014 University of Turku, Finland
[15] Institute for Astronomy, University of Edinburgh, Royal Observatory, Blackford Hill EH9 3HJ, UK
[16] Institute of Cosmology and Gravitation, University of Portsmouth, Portsmouth PO1 3FX, UK
[17] School of Physics and Astronomy, University of Southampton, Southampton, Hampshire SO17 1BJ, UK
[18] Instituto di Astrofisica e Planetologia Spaziali (INAF), Via Fosso del Cavaliere 100, Roma 00133, Italy
[19] The Oskar Klein Centre, Physics Department of Physics, Stockholm University, Albanova University Center, SE 106 91 Stockholm, Sweden
[20] Las Cumbres Observatory, 6740 Cortona Drive, Suite 102, Goleta, CA 93117-5575, USA
[21] Department of Physics, University of California, Santa Barbara, CA 93106-9530, USA
[22] Center for Astrophysics, Harvard & Smithsonian, 60 Garden Street, Cambridge, MA 02138-1516, USA
[23] School of Physics, Trinity College Dublin, The University of Dublin, Dublin 2, Ireland
[24] Astrophysics Research Centre, School of Mathematics and Physics, Queens University Belfast, Belfast BT7 1NN, UK
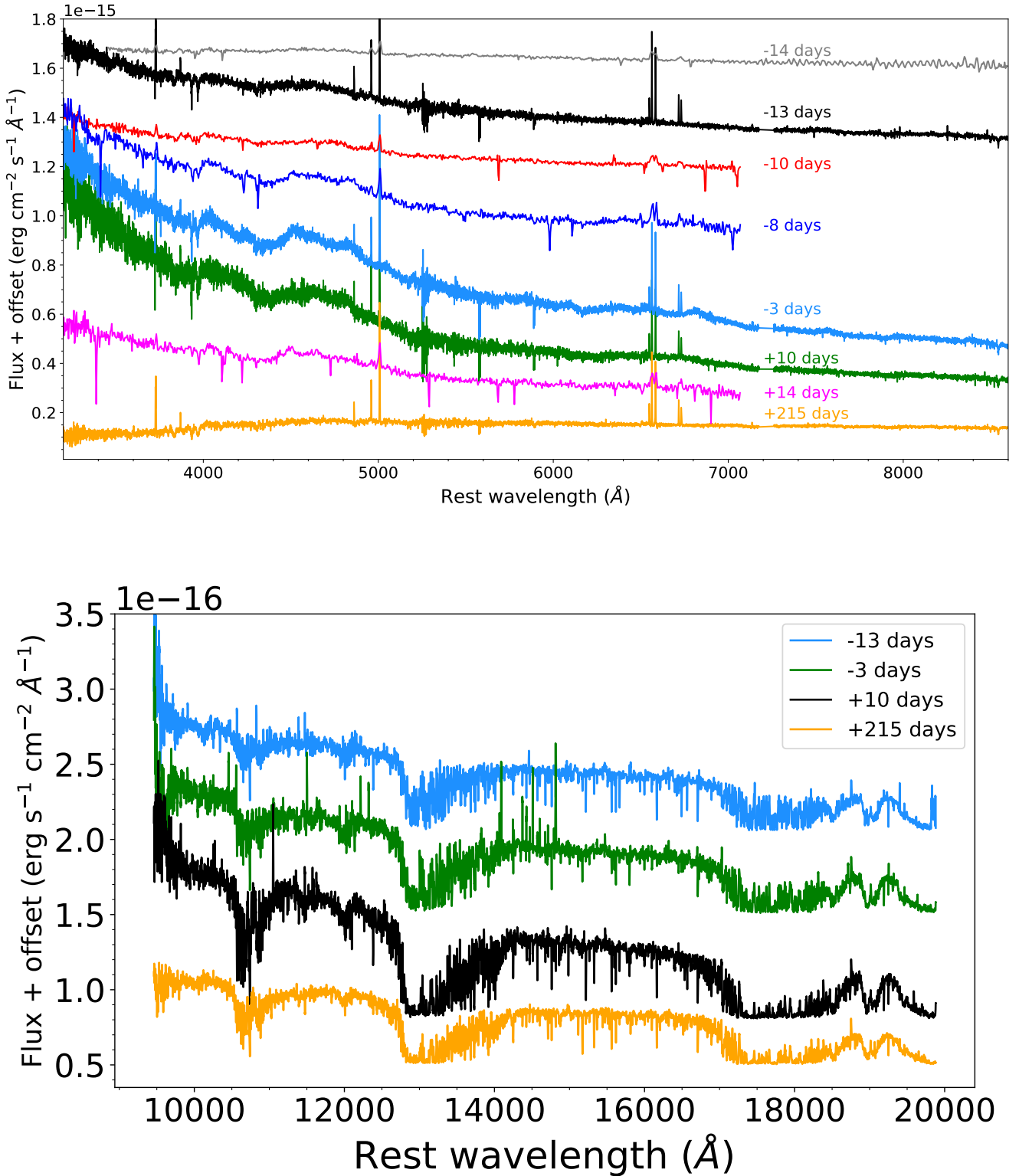
Appendix A: Figures

Fig. A.1. Flux-calibrated spectra of AT2020zso (top panel: visible wavelengths, bottom panel: NIR arm of X-shooter). The X-shooter spectra have been resampled to a 0.5 Å dispersion and offset for clarity.
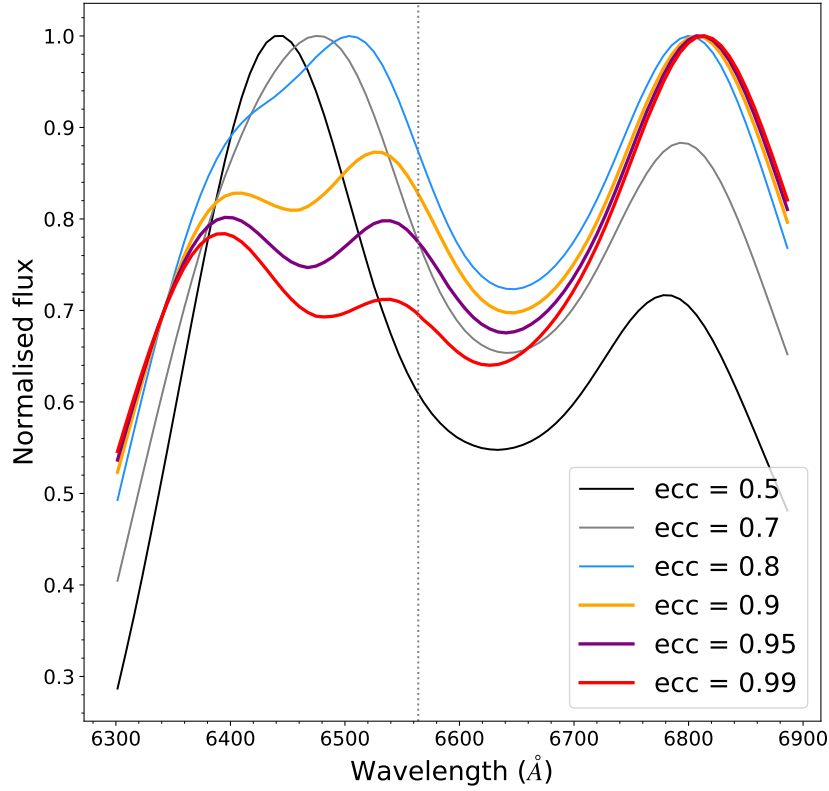
Fig. A.2. Illustration of the appearance of a large third middle bump with increasing eccentricity in the accretion disk model (all other disk parameters are similar to the ones inferred from the fitting). The dashed vertical line marks the rest wavelength, in this case Hα.
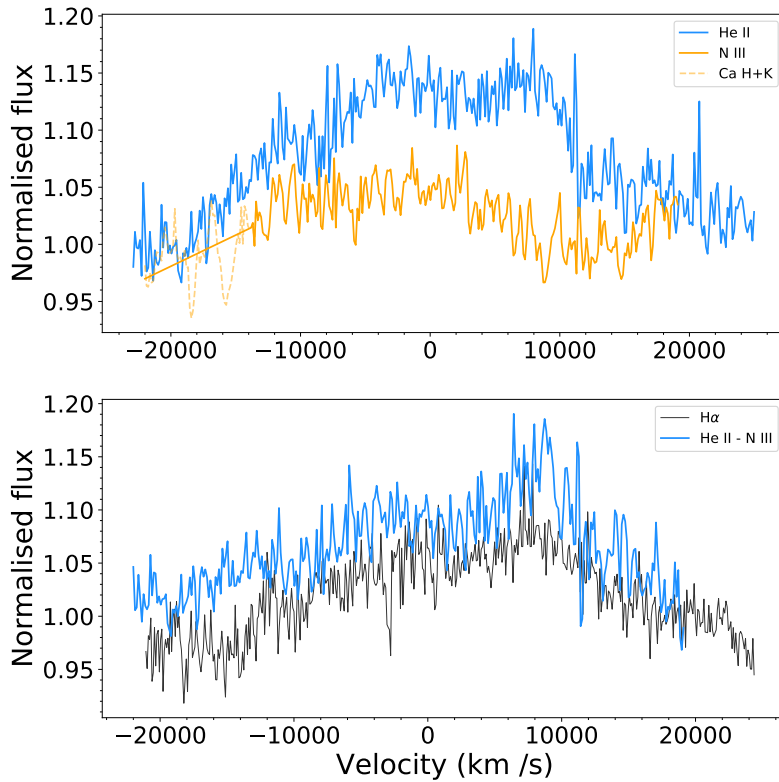
Fig. A.3. Comparison of the emission line profiles. Top panel: He II and N III profiles as observed at −3 days with X-shooter. The Ca H+K doublet is interpolated to avoid biasing the subtraction. Bottom panel: Subtracted profile (He II − N III) in blue, and Hα (black) for comparison.
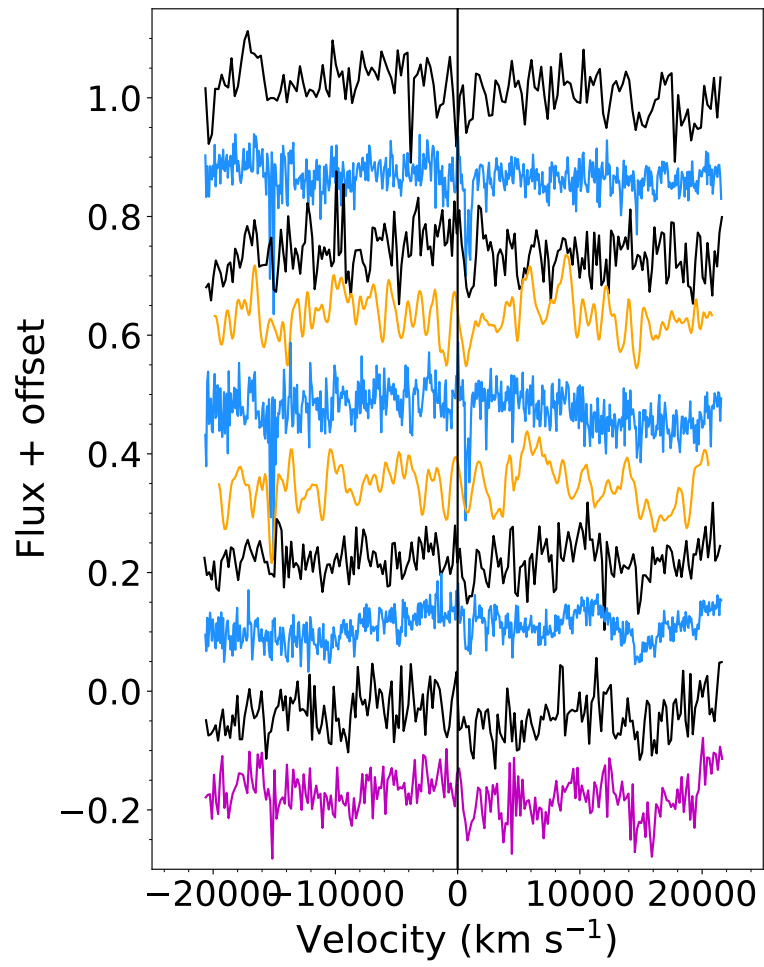
Fig. A.4. Same as Fig. 10 but for the He I line at 5876Å.
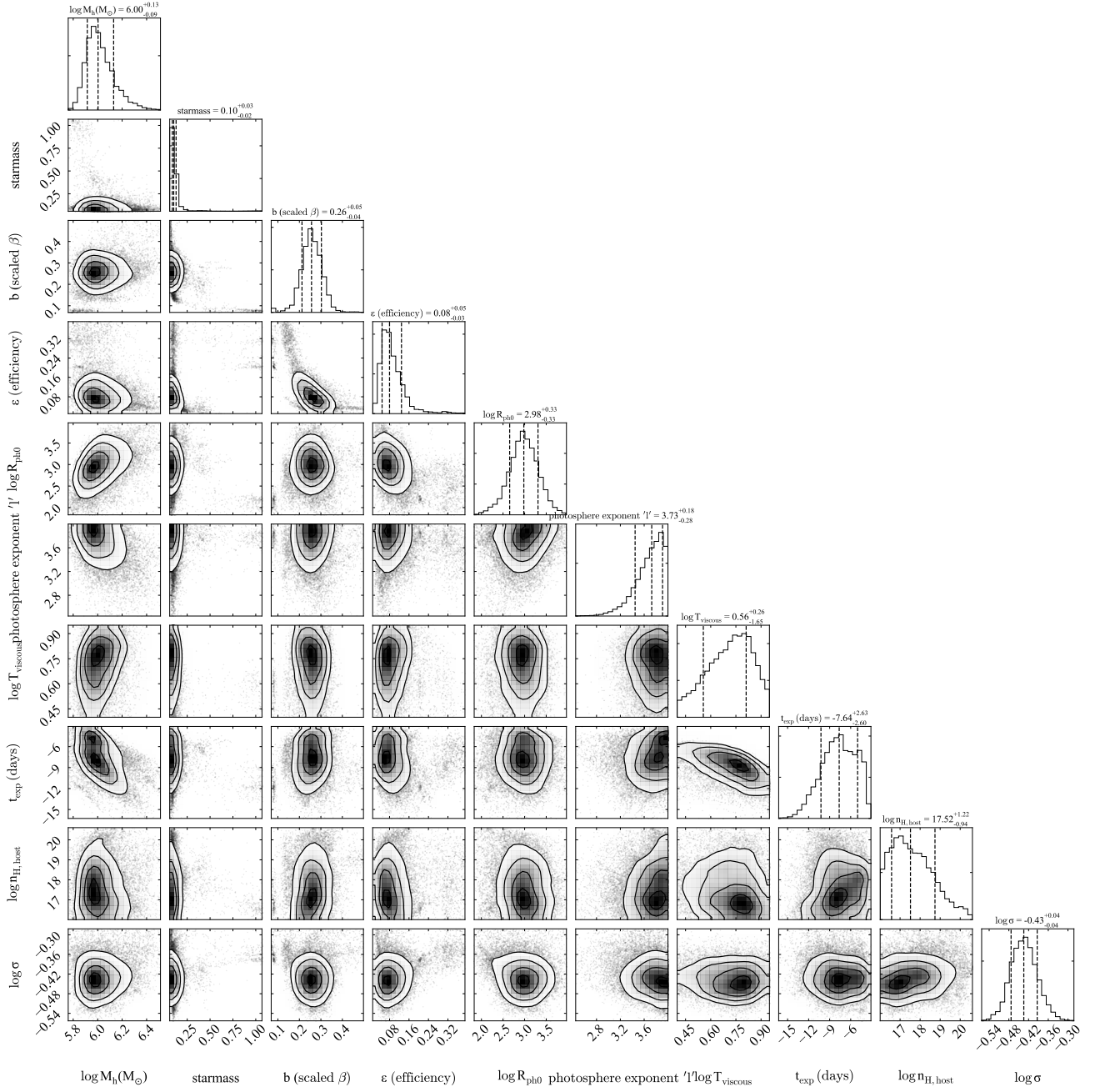
Fig. A.5. Full posterior distributions of the model parameter values for the light curve fitting with MOSFit.
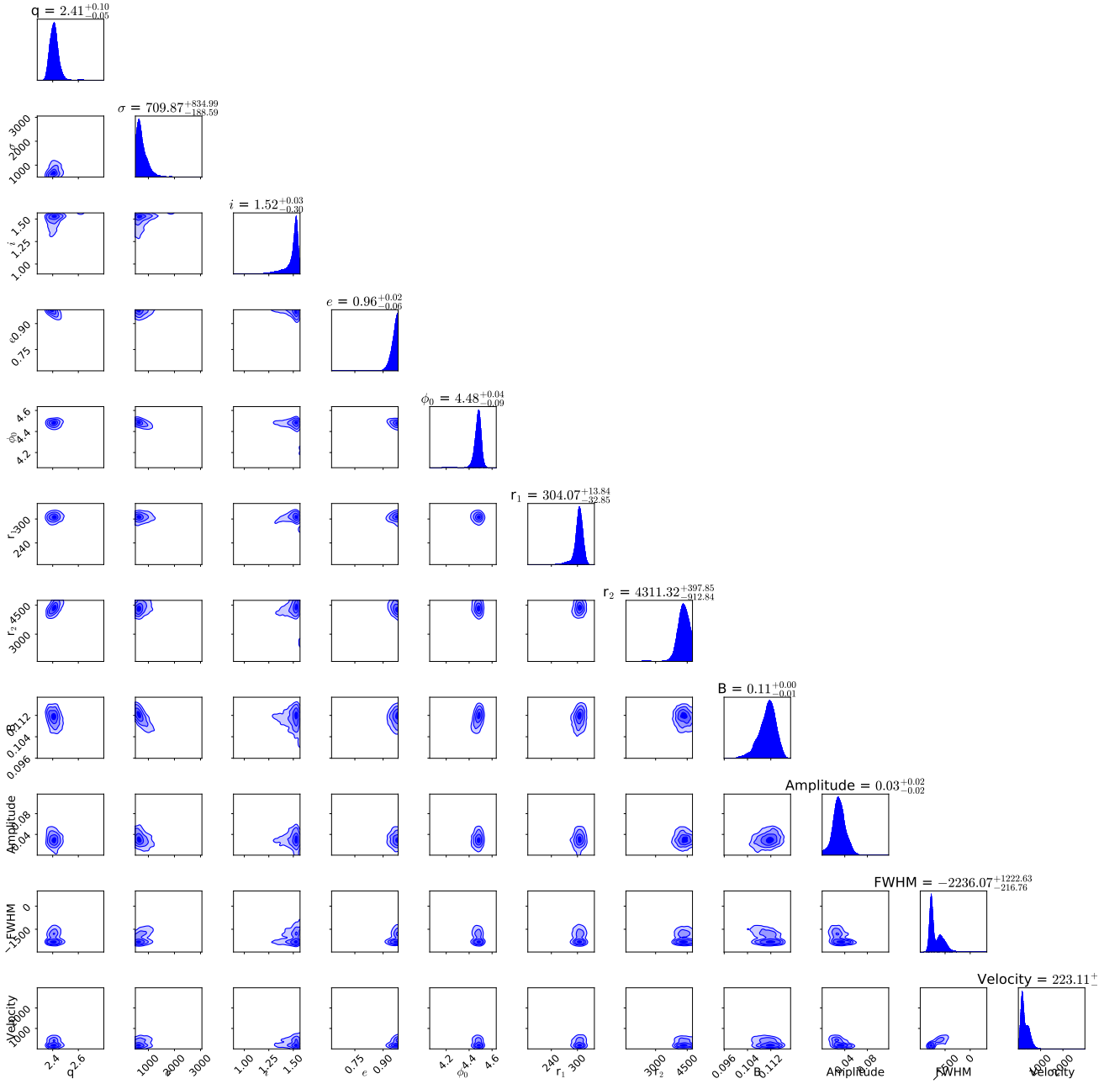
Fig. A.6. Full posterior distributions of the model parameter values for the Hα emission line (epoch –3 days). The inclination and orientation angle are sampled in units of radians. Note that to estimate parameter values and uncertainties, these samples need to be combined with their associated importance weights (and hence the values and uncertainties can differ from those reported in Table 5).
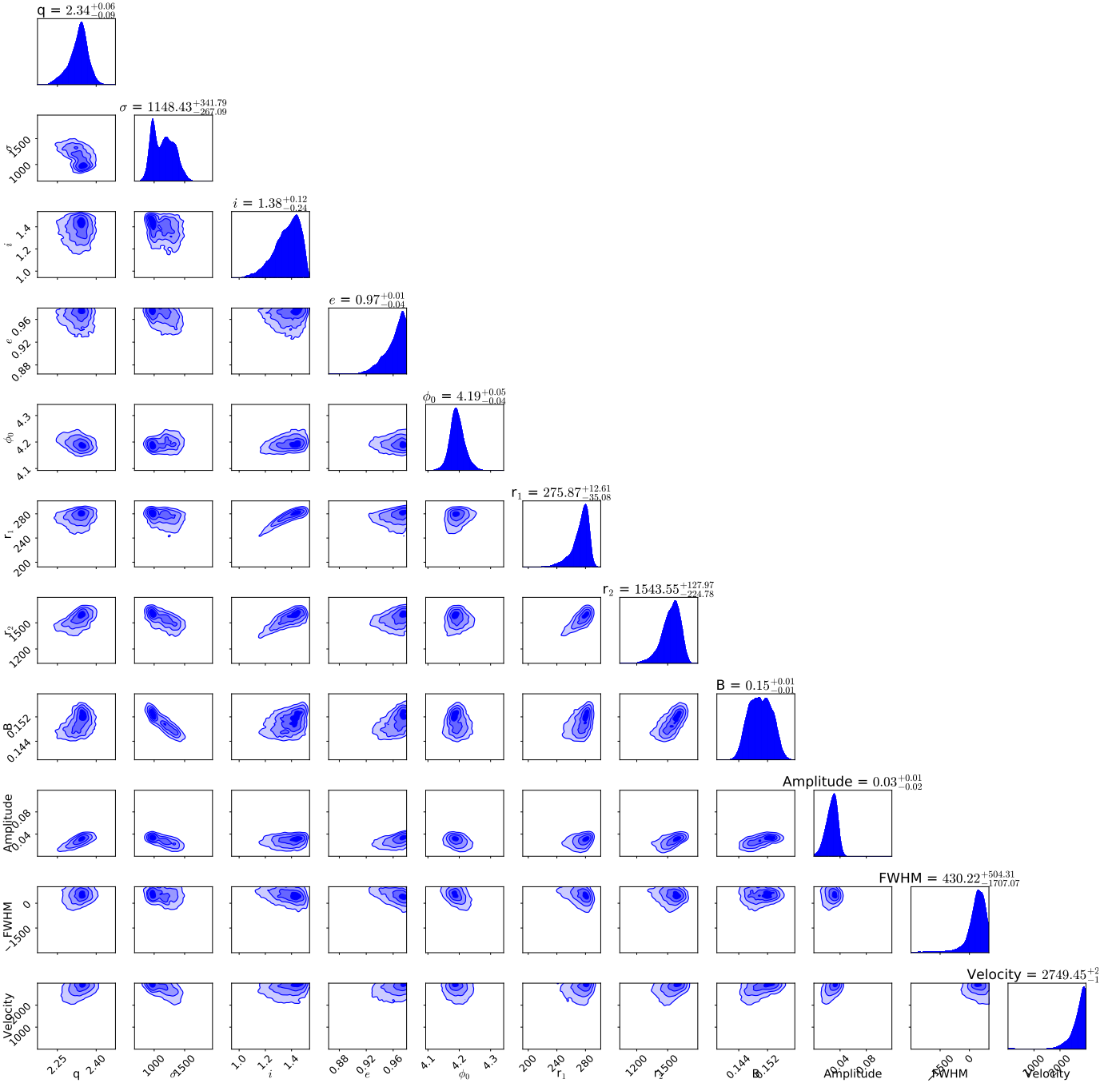
Fig. A.7. Full posterior distributions of the model parameter values for the Hα emission line (epoch +10 days). The inclination and orientation angle are sampled in units of radians. Note that to estimate parameter values and uncertainties, these samples need to be combined with their associated importance weights (and hence the values and uncertainties can differ from those reported in Table 5).
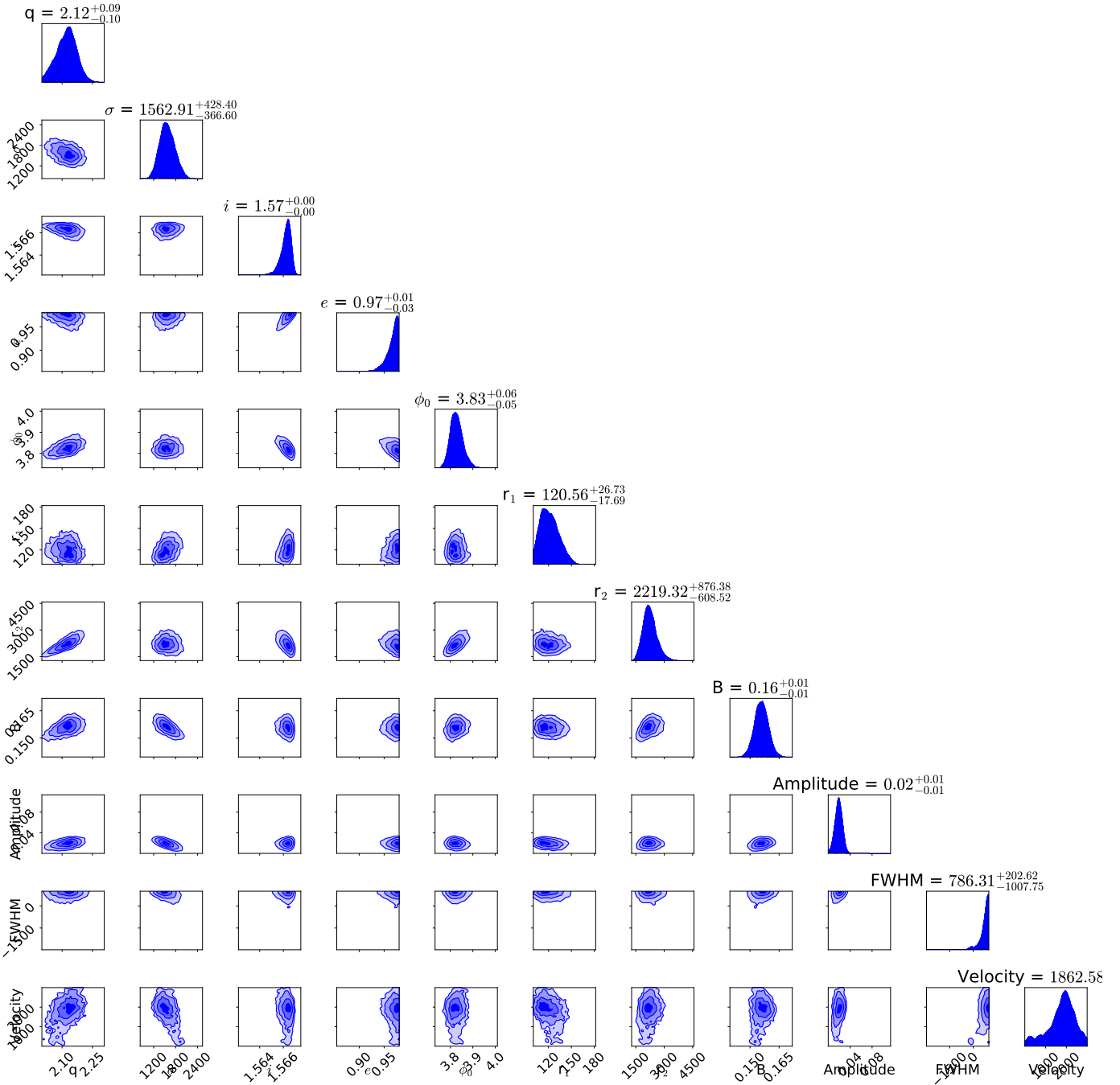
Fig. A.8. Full posterior distributions of the model parameter values for the (N III-subtracted) He II emission line (epoch −3 days). The inclination and orientation angle are sampled in units of radians. Note that to estimate parameter values and uncertainties, these samples need to be combined with their associated importance weights (and hence the values and uncertainties can differ from those reported in Table 5).

Fig. A.9. Full posterior distributions of the model parameter values for the (N III-subtracted) He II emission line (epoch +10 days). The inclination and orientation angle are sampled in units of radians. Note that to estimate parameter values and uncertainties, these samples need to be combined with their associated importance weights (and hence the values and uncertainties can differ from those reported in Table 5).
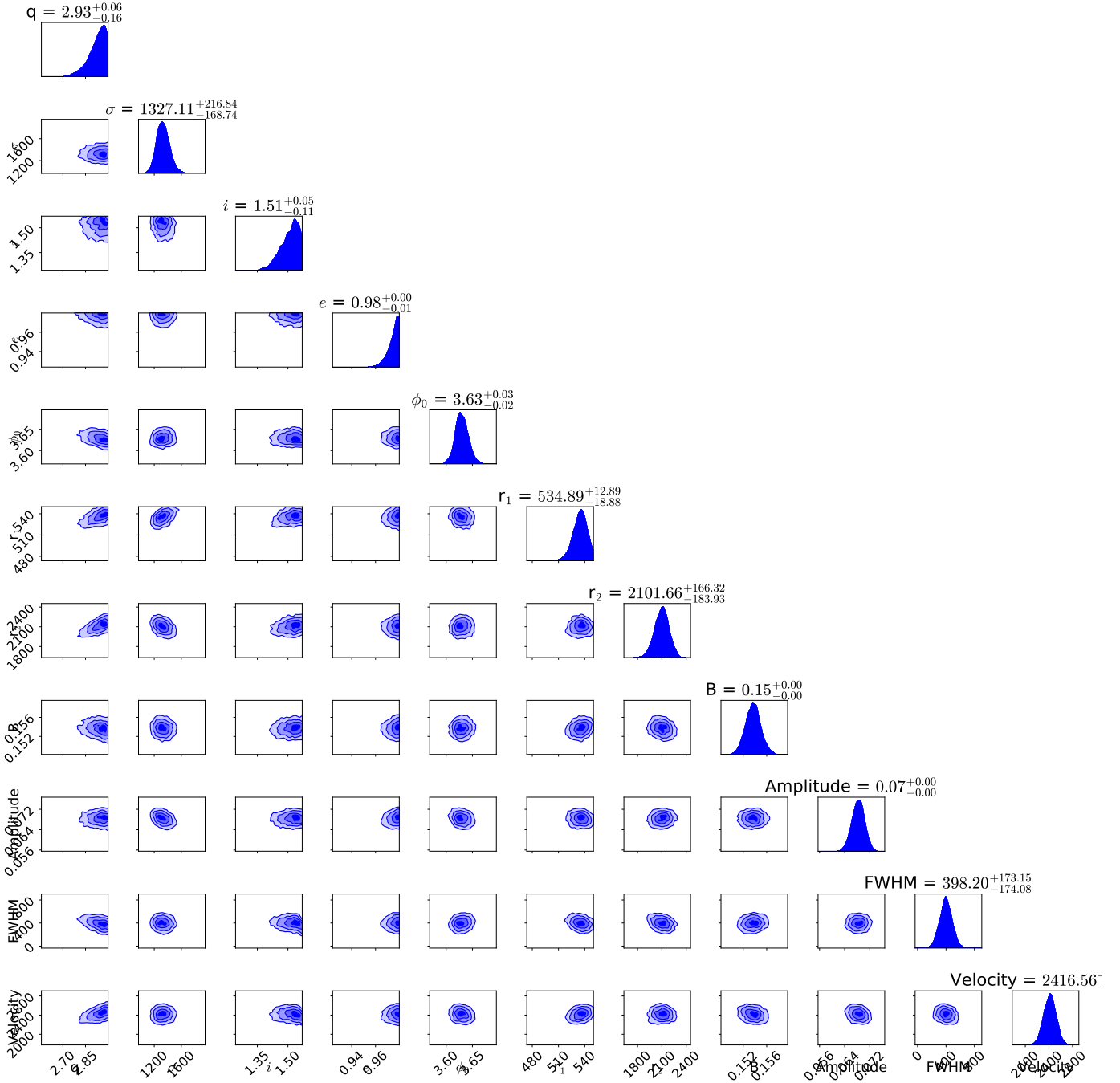
Appendix B: Photometry

Table B.1. Photometric observations of AT2020zso.

Telescope/filter	MJD	Magnitude	Uncertainty
ZTF/g	59165.150	20.40	0.23
ZTF/g	59167.188	20.15	0.25
ZTF/g	59168.101	19.69	0.16
ZTF/g	59170.164	19.00	0.10
ZTF/g	59172.117	18.56	0.08
ZTF/g	59178.158	18.29	0.09
ZTF/g	59182.155	18.03	0.09
ZTF/g	59184.149	17.98	0.07
ZTF/g	59189.110	17.65	0.05
ZTF/g	59192.187	17.58	0.13
ZTF/g	59194.181	17.78	0.10
ZTF/g	59197.109	17.64	0.23
ZTF/g	59199.149	17.93	0.09
ZTF/g	59205.097	18.53	0.08
ZTF/g	59205.097	18.53	0.08
ZTF/r	59165.086	20.87	0.24
ZTF/r	59167.193	20.43	0.19
ZTF/r	59168.167	20.13	0.15
ZTF/r	59170.108	19.21	0.10
ZTF/r	59178.198	18.37	0.08
ZTF/r	59182.197	18.21	0.07
ZTF/r	59187.170	17.92	0.06
ZTF/r	59189.170	17.83	0.07
ZTF/r	59199.124	18.13	0.08
ZTF/r	59205.130	18.42	0.08
ZTF/r	59205.130	18.42	0.08
ZTF/r	59211.141	18.73	0.15
Swift/V	59173.051	18.15	0.15
Swift/V	59173.179	17.52	0.13
Swift/V	59178.369	17.94	0.14
Swift/V	59180.227	18.17	0.25
Swift/V	59182.023	19.17	0.31
Swift/V	59184.207	19.83	0.34
Swift/V	59191.372	17.32	0.15
Swift/V	59195.758	17.33	0.14
Swift/V	59199.207	17.34	0.14
Swift/V	59204.724	17.93	0.18
Swift/V	59207.181	18.42	0.25
Swift/V	59211.497	19.44	0.35
Swift/V	59215.546	18.93	0.27
Swift/V	59327.786	19.77	0.28
Swift/V	59341.665	17.80	0.30
Swift/V	59355.871	20.08	0.22
Swift/B	59173.047	17.83	0.10
Swift/B	59173.175	17.78	0.12
Swift/B	59178.363	17.75	0.09
Swift/B	59180.224	17.59	0.14
Swift/B	59182.021	17.62	0.14
Swift/B	59184.204	17.91	0.17
Swift/B	59191.368	17.44	0.11
Swift/B	59195.753	17.55	0.10

Table B.1. Photometric observations of AT2020zso, continued.

Telescope/filter	MJD	Magnitude	Uncertainty
Swift/B	59199.202	17.79	0.12
Swift/B	59204.719	18.39	0.15
Swift/B	59207.177	18.24	0.16
Swift/B	59211.492	18.73	0.18
Swift/B	59215.541	18.58	0.18
Swift/B	59341.664	20.55	0.38
Swift/B	59355.865	20.17	0.18
Swift/U	59173.046	17.76	0.08
Swift/U	59173.174	18.09	0.11
Swift/U	59178.362	17.88	0.08
Swift/U	59180.224	17.79	0.13
Swift/U	59182.021	17.77	0.13
Swift/U	59184.204	17.71	0.13
Swift/U	59191.367	17.31	0.08
Swift/U	59195.752	17.62	0.09
Swift/U	59199.201	17.61	0.09
Swift/U	59204.718	18.41	0.12
Swift/U	59207.176	18.34	0.14
Swift/U	59211.491	18.78	0.16
Swift/U	59215.540	19.73	0.25
Swift/U	59321.217	19.94	0.25
Swift/U	59327.781	20.69	0.30
Swift/UVW1	59173.044	17.72	0.07
Swift/UVW1	59173.172	17.96	0.08
Swift/UVW1	59178.359	17.83	0.06
Swift/UVW1	59180.223	17.86	0.10
Swift/UVW1	59182.019	17.85	0.10
Swift/UVW1	59184.203	17.73	0.09
Swift/UVW1	59191.365	17.58	0.07
Swift/UVW1	59195.750	17.87	0.07
Swift/UVW1	59199.199	18.16	0.08
Swift/UVW1	59204.715	18.46	0.09
Swift/UVW1	59207.174	18.65	0.11
Swift/UVW1	59211.489	18.95	0.11
Swift/UVW1	59215.538	18.86	0.11
Swift/UVW1	59321.215	20.36	0.24
Swift/UVW1	59327.780	23.36	0.39
Swift/UVW1	59355.862	21.17	0.21
Swift/UVW2	59173.048	17.66	0.05
Swift/UVW2	59173.176	17.67	0.05
Swift/UVW2	59178.364	17.67	0.04
Swift/UVW2	59180.225	17.47	0.06
Swift/UVW2	59182.021	17.55	0.07
Swift/UVW2	59184.205	17.38	0.06
Swift/UVW2	59191.368	17.49	0.05
Swift/UVW2	59195.754	17.83	0.05
Swift/UVW2	59199.203	18.09	0.06
Swift/UVW2	59204.720	18.88	0.08
Swift/UVW2	59207.177	18.91	0.09
Swift/UVW2	59211.493	19.21	0.09
Swift/UVW2	59215.542	19.27	0.10
Swift/UVW2	59321.219	20.88	0.18
Swift/UVW2	59327.783	21.48	0.22

Table B.1. Photometric observations of AT2020zso, continued.

Telescope/filter	MJD	Magnitude	Uncertainty
Swift/UVW2	59341.664	20.44	0.25
Swift/UVW2	59355.866	20.98	0.16
Swift/UVM2	59173.052	17.91	0.08
Swift/UVM2	59173.180	17.81	0.07
Swift/UVM2	59178.371	17.80	0.05
Swift/UVM2	59180.227	17.74	0.07
Swift/UVM2	59182.024	17.65	0.07
Swift/UVM2	59184.207	17.48	0.06
Swift/UVM2	59191.373	17.49	0.05
Swift/UVM2	59195.759	17.80	0.05
Swift/UVM2	59199.208	17.94	0.05
Swift/UVM2	59204.725	18.72	0.07
Swift/UVM2	59207.181	18.69	0.08
Swift/UVM2	59215.547	19.02	0.08
Swift/UVM2	59321.224	20.49	0.21
Swift/UVM2	59327.787	20.73	0.24
Swift/UVM2	59341.666	21.28	0.29
Swift/UVM2	59355.872	21.50	0.16
LCO/B	59171.073	18.84	0.06
LCO/B	59171.076	18.86	0.05
LCO/V	59171.080	18.90	0.04
LCO/V	59171.083	18.96	0.05
LCO/g	59171.110	18.69	0.02
LCO/g	59171.114	18.69	0.02
LCO/r	59171.118	18.85	0.03
LCO/r	59171.121	18.89	0.04
LCO/i	59171.124	18.91	0.06
LCO/i	59171.126	18.86	0.05
LCO/B	59174.059	18.48	0.09
LCO/V	59174.067	18.54	0.04
LCO/g	59177.149	18.20	0.04
LCO/g	59177.153	18.41	0.06

Table B.1. Photometric observations of AT2020zso, continued.

Telescope/filter	MJD	Magnitude	Uncertainty
LCO/r	59177.157	18.55	0.11
LCO/B	59178.094	18.09	0.08
LCO/B	59178.097	18.26	0.08
LCO/i	59180.074	18.29	0.06
LCO/B	59180.417	18.27	0.04
LCO/B	59180.421	18.27	0.04
LCO/V	59180.425	18.33	0.04
LCO/V	59180.427	18.17	0.05
LCO/g	59185.420	17.94	0.04
LCO/g	59185.424	17.89	0.02
LCO/g	59188.775	17.77	0.01
LCO/g	59188.779	17.66	0.01
LCO/r	59188.783	18.04	0.04
LCO/r	59188.785	17.76	0.01
LCO/i	59188.788	17.74	0.02
LCO/i	59188.791	17.70	0.03
LCO/B	59191.777	17.83	0.03
LCO/B	59193.778	17.92	0.03
LCO/B	59193.782	17.90	0.03
LCO/V	59193.786	17.82	0.03
LCO/V	59193.788	17.88	0.02
LCO/B	59210.054	18.86	0.12
LCO/B	59210.058	18.71	0.10
LCO/V	59210.062	18.77	0.13
LCO/V	59210.065	18.76	0.11
LCO/g	59219.045	19.26	0.07
LCO/g	59219.049	19.23	0.05
LCO/r	59219.053	19.29	0.06
LCO/r	59219.056	19.29	0.06
LCO/i	59219.058	18.99	0.07
LCO/i	59219.061	18.88	0.09